Experimental constraints on ureilite petrogenesis

Steven Singletary *, Timothy L. Grove

Department of Earth, Atmospheric and Planetary Sciences, Massachusetts Institute of Technology, Cambridge, MA 02139, USA

Abstract

This experimental study explores the petrogenesis of ureilites by a partial melting/smelting process. Experiments have been performed over temperature (1150–1280 °C), pressure (5–12.5 MPa), and low oxygen fugacity (graphite–CO gas) conditions appropriate for a hypothetical ureilite parent body ~200 km in size. Experimental and modeling results indicate that a partial melting/smelting model of ureilite petrogenesis can explain many of the unique characteristics displayed by this meteorite group. Compositional information preserved in the pigeonite–olivine ureilites was used to estimate the composition of melts in equilibrium with the ureilites. The results of 20 experiments saturated with olivine, pyroxene, metal, and liquid with appropriate ureilite compositions are used to calibrate the phase coefficients and pressure–temperature dependence of the smelting reaction. The calibrated coefficients are used to model the behavior of a hypothetical residue that is experiencing fractional smelting. The residue is initially olivine-rich and smelting progressively depletes the olivine content and enriches the pyroxene and metal contents of the residues. The modeled residue composition at 1260 °C best reproduces the trend of ureilite bulk compositions. The model results also indicate that as a ureilite residue undergoes isothermal decompression smelting over a range of temperatures, Ca/Al values and Cr_2O_3 contents are enriched at lower temperatures (below ~1240 °C) and tend to decrease at higher temperatures. Therefore, fractional smelting can account for the high Ca/Al and Cr_2O_3 wt% values observed in ureilites. We propose that ureilites were generated from an olivine-rich, cpx-bearing residue. Smelting began when the residue was partially melted and contained liquid, olivine, and carbon. These residues experienced varying degrees of fractional smelting to produce the compositional variability observed within the pigeonite-bearing ureilites. Variations in mineral composition, modal proportions, and isotopic signatures are best described by heterogeneous accretion of the ureilite parent body followed by minimal and variable degrees of igneous processing.
© 2005 Elsevier Inc. All rights reserved.

1. Introduction

Ureilites are primitive achondrites that consist of olivine, pyroxene, and carbon. They represent the second largest achondrite group but their petrogenesis remains enigmatic. Ureilites display equilibrated coarse-grained textures and mineral chemistry but retain primordial gas contents and isotope signatures.

A wide variety of models have been put forward to explain ureilite petrogenesis. Goodrich et al. (1987) developed a multi-stage cumulate model based on mineral chemistry

and textures. In the model, ureilites represent cumulates from a magma generated by <10% partial melting of a plagioclase-depleted source that had superchondritic Ca/Al ratios. Ureilites would therefore represent only a small fraction of the amount of material that was processed. The most likely precursor materials, carbonaceous chondrites, do not have superchondritic Ca/Al ratios and formation of the ureilites from them would require more than one melting event. Since ureilites are the second most abundant achondrite, the complementary material should be present in our collections. No meteorite type complementary to the ureilites, either residues of the original partial melting or the subsequent basaltic magma left after ureilite accumulation, has been described (Rubin, 1988).

Residue models to explain the ureilites have also been proposed (Boynton et al., 1976; Wasson et al., 1976; Scott

---

* Corresponding author. Present address: Department of Natural Sciences, Fayetteville State University, Fayetteville, NC 28301, USA. Fax: +1 910 672 1159.

E-mail address: ssingletary@uncfsu.edu (S. Singletary).

et al., 1993). A difficulty for these models is accounting for the strong mineral alignments observed in some ureilites (Berkley et al., 1980; Rubin, 1988) that suggest a cumulate origin. However, experimental evidence suggests fabrics can be produced in a residue by thermal compaction (Walker and Agee, 1988). The high carbon content of the ureilites was accounted for by impact of a carbon-rich body. However, this does not explain the presence of carbide-bearing spherules (up to 100 μm) within olivine (Goodrich and Berkley, 1986) or the presence of large, bladed graphite crystals in low shock ureilites (Berkely and Jones, 1982).

Takeda (1987) proposed that ureilites represent nebular condensates that underwent high temperature recrystallization during the early stages of planetesimal collision. If this was the case, ureilites should have higher sulfur contents than they do (Rubin, 1988), as sulfide melts do not readily separate from a crystalline silicate melt (Walker and Agee, 1988).

Smelting of an olivine-rich source has also been suggested as a petrogenetic process to account for the ureilites (Walker and Grove, 1993). The amount of smelting is controlled by C–O–Fe equilibria which are strongly pressure dependent. At low pressures (2.5 MPa) FeO in silicates is unstable and is reduced to Fe metal, producing MgO-rich silicates and a CO gas. Above 10 MPa smelting is suppressed and Fe silicates coexist with graphite (Walker and Grove, 1993). Therefore, the less smelted ureilite samples record greater pressures in the parent body, and the more smelted samples record lower pressure. Many authors have argued that if smelting had occurred, there should exist correlations between the modal percentage of pyroxene, metal content, and mg# (defined here as molar MgO/[MgO + FeO]) (e.g., Goodrich, 1992; Mittlefehldt et al., 1998). Singletary and Grove (2003) established this correlation using a quantitative petrologic study of 21 ureilites.

2. Ureilite petrography and petrology

The typical ureilite texture is characterized by elongated, anhedral pyroxene and olivine grains ∼1 mm in size with curved intergranular boundaries that generally meet in triple junctions. Pigeonite, augite, and orthopyroxene all occur in ureilites; however, pigeonite is the sole pyroxene in ∼77% of ureilites (Mittlefehldt et al., 1998). Where pigeonite is the sole pyroxene present, it shows no exsolution lamellae and is inferred to have cooled rapidly from high temperature. Augite is present in ∼10% of ureilites as small irregular blebs and lamellae in pigeonite and as larger, discrete crystals. Orthopyroxene is also present in a small number of ureilites, predominantly as large crystals poikilitically enclosing other pyroxenes (Takeda et al., 1989).

Olivine in ureilites ranges in composition from Fo_{74} to Fo_{95} and is characterized by high Cr_2O_3 (∼0.56–0.85 wt%) and CaO (∼0.30–0.45 wt%) contents (Mittlefehldt et al., 1998). A characteristic feature of the ureilites is the presence of reduced rims on olivine where in contact with the carbon-

rich matrix and where crosscut by veins of carbon-bearing material (Berkley et al., 1980). The rims are most prominent on olivine, but can be observed on other silicate phases to varying degrees. The olivine rims are composed of nearly pure forsterite, Ni-free metal blebs, and enstatite. The rims vary in width from 10 to 100 μm and display sharp contacts with the interior of the grains (Mittlefehldt et al., 1998). The rims are hypothesized to be a feature produced late in ureilite petrogenesis at fairly high temperature (∼1100 °C) (Sinha et al., 1997).

Carbon occurs predominantly as fine-grained graphite in an interstitial matrix that also contains fine-grained silicates, metal, sulfides, and phosphides (Mittlefehldt et al., 1998). Rare, mm-sized euhedral graphite crystals have been observed in some ureilites (Treiman and Berkley, 1994). Other polymorphs of carbon that have been identified in ureilites include diamond and lonsdaleite as well as chaoite and organic compounds (Vdovykin, 1970).

The olivine and pyroxene core compositions are homogeneous within grains and between grains in a single meteorite in terms of mg#. However, between meteorites, significant variability exists in mineral chemistry and modal proportions. Olivine forsterite contents range from 74 to 95 with coexisting pyroxenes having mg#s in the same range, indicating Fe–Mg equilibrium between olivine and pyroxene (Mittlefehldt et al., 1998). The modal percent pigeonite varies from 0% in LEW86216 to 100% in MET 01085. A correlation of increasing modal percent pigeonite with higher silicate mg# was reported by Singletary and Grove (2003) and is hypothesized to result from a primary, low-pressure partial melting/smelting event in the presence of carbon.

A long standing debate on ureilite petrogenesis has centered on whether the rocks represent the residues of a partial melting process or a cumulate pile resulting from fractional crystallization of a large body of magma on the ureilite parent body. The meteorites are very coarse-grained, containing olivine and pigeonite that average from 1 to 3 mm in length, with grains as large as 15 mm (Mittlefehldt et al., 1998). The grain boundaries are smooth and curved with abundant 120° triple junctions (Goodrich, 1992). In some ureilites, the silicate grains are elongate and the long crystal axes define weak foliations and lineations (Berkley et al., 1976, 1980). In spite of textures that might indicate extensive processing and equilibrated mineral compositions, the ureilites retain several geochemical characteristics of primitive, unprocessed nebular material.

An alternative model to explain the modal and mineralogical variations is that the characteristics are nebular in origin (Takeda, 1987). Several geochemical characteristics of the ureilites have been used to support this hypothesis. The most striking primitive characteristic is the oxygen isotope signature. Ureilites plot along a line of slope 1 that is defined by end members of carbonaceous chondrite and anhydrous minerals (CCAM) (Clayton and Mayeda, 1988, 1996) (Fig. 1). Any high temperature, planetesimal-scale igneous process should fractionate the oxygen iso-
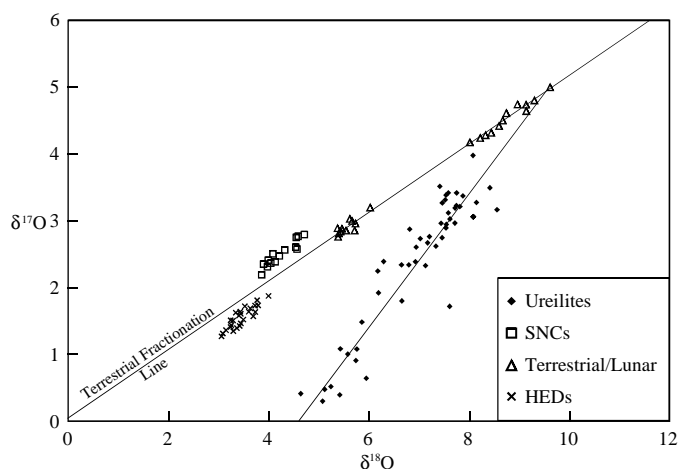
Fig. 1. $\delta^{17}O$ versus $\delta^{18}O$ of martian, HED, terrestrial, lunar, and ureilite samples. Ureilites lie along a line of slope 1. The terrestrial fraction line has slope 0.52 and is characteristic of samples that have undergone extensive igneous processing. The martian samples also fall along a line of slope 0.52 but displaced from the terrestrial fractionation line. Data from Clayton and Mayeda (1996).

topes such that they lie along a line with slope of 0.52 (i.e., the lines defined by samples of Mars, Moon, Earth, and 4 Vesta). Ureilites also retain noble gases in chondritic abundances (Weber et al., 1976). The oxygen isotopic signature and noble gas abundances suggest that ureilites have experienced minimal amounts of processing. The key to ureilite petrogenesis lies in reconciling the overwhelming petrographic evidence that suggests extensive igneous processing with these primitive geochemical characteristics.

Here, we present new experimental results to constrain the amount of processing required to generate the ranges of mineral chemistry and modal proportions observed in ureilites. We hypothesize that olivine–pigeonite-bearing ureilites represent the residues of partial melting. The presence of carbon and low pressures on the ureilite parent body combined to create an environment in which a smelting reaction occurred. Smelting for the purposes of this discussion is defined as the reaction:

$$olivine + liquid + carbon \rightarrow pigeonite + Fe\ metal + CO\ gas \tag{1}$$
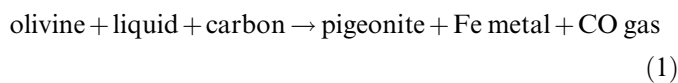
As the reaction proceeds, Fe metal is sequestered and the mg# of the major silicate phases rises. We posit that the relationship of modal percent pigeonite and mg# reported by Singletary and Grove (2003) is a consequence

of this reaction. Petrologic modeling using the experimental data also suggests smelting may be responsible for the high olivine Cr_2O_3 contents and enriched Ca/Al ratios observed in ureilites.

3. Procedures

All experiments reported here were performed in the MIT Experimental Petrology Laboratory. The bulk compositions used in the experiments are given in Table 1. Experimental run conditions and products are reported in Table 2. For this study, five bulk compositions were selected (see Section 6).

The starting material was prepared by mixing together high purity reagent grade oxides and Fe° sponge (Grove and Bence, 1977). Grinding under ethanol for ~6 h produced a uniform powder. Approximately 10–15 mg of the starting powder was packed into a handcrafted carbon capsule. The carbon capsule was then inserted into a platinum tube that was welded shut on one end and loosely crimped on the other. A small hole was made in the crimped end to ensure full transmission of the imposed CO gas pressure to the interior of the experimental charge. The finished assembly, with the welded end at the bottom, was loaded into the pressure vessel.

The experiments were performed in a rapid quench, externally heated, ZHM alloy, cold seal pressure vessel contained in an inconel 600 sheath. The pressure vessel has an inner diameter of 0.25 in. and was surrounded by argon to prevent oxidation. Once sealed, the vessel is pressurized with CO gas, that serves both as the pressure medium and to ensure a reducing environment. The vessel is then placed in a vertical Del Tech furnace and brought to run temperature. At the end of the experiment, the vessel is extracted from the furnace and inverted to drop the experimental charge to the cold region of the vessel. Rapping the end of the pressure vessel with a wrench assists in making sure the charge falls to the cooling head.

Experiments were then removed from the pressure vessel and extracted from the Pt tube and carbon capsule. Frequently, the experiment would come out as one coherent glass bead, other times as a loose aggregate of glass beads and crystals. The bead(s) and/or crystals were then crushed in a Plattner mortar and mounted in epoxy. The mounts were then polished and carbon coated for microprobe analysis (see Fig. 2 for examples of prepared experimental products).

Table 1
Synthetic bulk compositions used in this study

	SiO_2	TiO_2	Al_2O_3	Cr_2O_3	FeO	MnO	MgO	CaO
Pu	54.09	0.52	6.56	0.76	14.36	0.21	9.80	13.72
$Pu + Fo_{83.8}$	49.95	0.37	4.65	0.54	14.67	0.15	19.94	9.74
$Pu + Fo_{75}$	49.54	0.37	4.65	0.54	16.84	0.15	18.17	9.74
ULM	50.64	0.57	11.97	0.68	14.50	0.32	9.59	11.74
$ULM + Fo_{75}$	48.19	0.45	9.57	0.54	16.18	0.25	15.41	9.40
$ULM + Fo_{75} + Cpx$	48.46	0.66	9.08	0.51	15.61	0.24	15.24	10.20

Table 2
Experimental run conditions and results

Exp # (bulk)	t (h)	P (bars)	T (°C)	Phase (#analysis)	% phase	SiO$_2$	TiO$_2$	Al$_2$O$_3$	Cr$_2$O$_3$	FeO	MnO	MgO	CaO	Total	mg#	$K_D^{phase/liq}$	SSR
Pu-12	13	125	1260	Ol (10)[a]	0.161	39.3(3)[b]	—[c]	—	0.39(2)	17.2(3)	0.15(2)	43.1(2)	0.49(3)	100.63	81.8	0.34	0.0056
Pu + Fo$_{83.8}$				Pig (12)	0.164	56.3(6)	—	0.4(3)	0.56(9)	10.8(2)	0.13(2)	29.0(8)	3.9(6)	101.09	82.8	0.32	
				Glass (8)	0.66	52.1(2)	0.51(3)	6.9(1)	0.54(1)	14.7(2)	0.16(2)	12.5(2)	13.7(2)	101.11	60.3		
Pu-14	15	125	1230	Oliv (16)	0.374	38.8(4)	—	—	0.37(3)	19.0(3)	0.15(3)	41.5(5)	0.51(9)	100.33	79.6	0.32	0.0082
Pu + Fo$_{83.8}$				Aug (2)	—	50.8(1)	0.69(5)	5.8(2)	0.87(3)	12.4(6)	0.12(1)	15.0(9)	15(2)	100.68	68.4	0.57	
				Pig (13)	0.286	55.6(3)	0.07(3)	0.47(8)	0.57(6)	11.4(3)	0.14(3)	26.7(5)	5.9(7)	100.85	80.6	0.32	
				Glass (33)	0.341	50.5(3)	0.63(7)	8.1(1)	0.46(3)	15.2(3)	0.18(2)	10.5(6)	14.1(4)	99.67	55.2		
Pu-15	8	125	1280	Oliv (5)	0.431	39.6(3)	—	—	0.39(3)	15.6(2)	0.12(3)	44.1(4)	0.45(2)	100.26	83.5	0.33	0.0125
Pu + Fo$_{83.8}$				Pig (7)	0.026	56.9(3)	0.06(1)	0.30(4)	0.55(2)	9.7(3)	0.16(2)	30.0(7)	3.5(3)	101.17	84.6	0.31	
				Glass (50)	0.546	52.3(2)	0.43(5)	6.41(7)	0.56(3)	13.9(2)	0.14(2)	13.1(1)	12.8(1)	99.64	62.7		
Pu-17	16	50	1260	Pig (22)	0.473	56.5(4)	0.10(3)	0.5(3)	0.58(5)	7(1)	—	30(2)	6(2)	100.68	88.8	0.36	0.3655
Pu + Fo$_{83.8}$				Aug (17)	0.021	55.5(6)	0.15(4)	0.5(1)	0.50(4)	4.0(9)	—	24(2)	15(3)	99.65	91.6	0.26	
				Glass (15)	0.423	54.8(3)	1.3(3)	9.1(2)	—	7.6(4)	0.14(7)	12.0(5)	15.2(2)	100.14	73.8		
				Metallic iron	0.084												
Pu-19	11	100	1260	Oliv (8)	0.136	39.8(3)	—	—	0.37(2)	15.8(3)	0.17(3)	43.9(4)	0.50(4)	100.54	83.2	0.33	0.0238
Pu + Fo$_{83.8}$				Pig (21)	0.225	56.6(6)	0.06(2)	0.38(9)	0.51(4)	9.1(5)	0.09(3)	28.9(7)	4.8(5)	100.44	84.9	0.29	
				Glass (54)	0.617	52.0(2)	0.47(5)	7.5(1)	0.43(4)	13.5(2)	0.05(3)	12.3(1)	14.0(2)	100.25	61.9		
				Metallic iron	0.022												
Pu-20	24	100	1230	Pig (18)	0.289	55.7(2)	0.07(2)	0.5(1)	0.52(4)	11.3(5)	0.17(2)	26.3(5)	6.3(7)	100.86	80.6	0.30	0.039
Pu + Fo$_{83.8}$				Oliv (14)	0.162	38.7(2)	—	—	0.35(1)	19.6(3)	0.16(1)	40.6(2)	0.54(5)	99.95	78.8	0.33	
				Glass (18)	0.544	50.7(2)	0.7(1)	8.5(1)	0.40(7)	15.1(3)	0.17(7)	10.5(2)	14.2(1)	100.27	55.4		
				Metallic iron	t[e]												
Pu-22	28	80	1230	Pig (12)	0.546	56.3(5)	0.11(2)	0.6(1)	0.59(6)	9.1(6)	0.20(3)	27.9(8)	6.1(6)	100.90	84.6	0.28	1.689
Pu + Fo$_{83.8}$				Glass (43)	0.404	51.4(3)	0.6(1)	0.7(2)	0.45(8)	12.5(4)	0.14(4)	10.8(2)	14.5(2)	100.09	60.5		
				Metallic iron	0.050												
Pu-30	21	75	1260	Aug (6)	0.098	55.1(2)	0.10(2)	0.26(4)	0.52(5)	5.7(5)	0.15(2)	21.9(8)	16(1)	99.73	87.2	0.28	0.4011
Pu + Fo$_{75}$				Pig (5)	0.344	56.3(9)	0.08(1)	0.44(2)	0.57(5)	7.0(3)	0.15(2)	31.2(6)	4.3(6)	100.04	88.8	0.24	
				Glass (14)	0.467	55.2(3)	0.5(1)	9(2)	0.4(2)	10(1)	0.15(4)	11(3)	14.1(5)	100.35	63.9		
				Metallic iron	0.092												
ULM-1	16	115	1260	Pig (4)	0.018	55.7(3)	0.07(2)	0.47(6)	0.9(2)	9.5(4)	0.40(3)	29.3(5)	3.1(5)	99.44	84.6	0.26	0.7758
ULM				Glass (20)	0.946	53.2(4)	0.5(1)	12.0(2)	0.60(7)	11.5(3)	0.39(7)	9.2(2)	12.4(3)	99.79	58.7		
				Metal	0.036												
ULM-2	26	115	1200	Glass (24)	0.981	50.1(3)	0.6(2)	13.4(2)	0.39(4)	12.6(3)	0.40(5)	9.0(2)	13.2(2)	99.69	55.9		4.9990
ULM				Metal	0.019												
ULM-5	24	110	1180	Glass (34)	0.720	48.0(3)	0.4(1)	12.6(1)	0.22(6)	15.5(5)	0.31(5)	7.8(4)	12.7(3)	97.53	47.3		0.2540
ULM + Fo$_{75}$				Olivine (11)	0.192	37.2(7)	—	0.02(1)	0.18(1)	24(3)	0.28(1)	37(3)	0.43(2)	99.11	72.8	0.33	
				Opx (14)	0.107	52.9(6)	0.10(1)	0.9(3)	0.63(7)	18(3)	0.27(3)	23(2)	3.1(4)	98.90	70.0	0.38	
				Metal	−0.018												
ULM-8	20	120 b	1230	Glass (50)	0.886	51.3(3)	0.48(5)	11.0(1)	0.43(3)	15.5(2)	0.22(3)	11.1(2)	10.5(1)	100.53	56.2		0.0887
ULM + Fo$_{75}$				Olivine (16)	0.184	38.8(6)	0.03(2)	0.05(1)	0.35(2)	19.5(3)	0.26(2)	41.3(9)	0.36(2)	100.65	79.1	0.34	
				Opx (34)	−0.070	56.2(6)	0.08(3)	1.0(5)	0.72(7)	12.5(4)	0.21(3)	28.2(9)	1.8(3)	100.71	80.2	0.32	

ULM-9 *ULM + Fo75*	11	110	1300	Glass (21)	0.854	49.7(3)	0.59(5)	11.0(1)	0.43(4)	15.0(4)	0.24(3)	11.6(6)	11.1(4)	99.66	57.9		0.0467
				Olivine (7)	0.111	39.2(4)	0.01(1)	0.05(3)	0.37(5)	16.9(4)	0.23(2)	43.1(7)	0.37(2)	100.23	81.9	0.30	
				Opx (4)	0.023	56.4(2)	0.03(1)	0.33(1)	0.51(2)	12.1(6)	0.22(4)	29.7(5)	1.1(1)	100.39	81.2	0.32	
				Metal	0.012	—	—	—	—	—	—	—	—				
ULM-10 *ULM + Fo75*	12	75	1230	Glass (85)	0.742	50.2(9)	0.56(7)	12.2(7)	0.50(4)	10.5(4)	0.29(3)	12.2(2)	12.6(6)	99.05	67.4		0.3134
				Olivine (12)	0.177	39.6(8)	0.01(1)	0.03(1)	0.39(2)	13.2(4)	0.27(3)	46(1)	0.34(4)	99.84	86.1	0.34	
				Opx (24)	0.015	56.6(7)	0.05(2)	0.5(1)	0.58(5)	8.3(6)	0.30(4)	31.4(6)	2.1(2)	99.83	87.0	0.31	
				Metal	0.066	—	—	—	—	—	—	—	—				
ULM-11 *ULM + Fo75*	18	115	1200	Glass (70)	0.759	49.8(3)	0.7(1)	12.6(2)	0.26(7)	13.9(4)	0.27(5)	9.1(4)	12.5(2)	99.13	53.8		0.0840
				Olivine (13)	−0.138	38.2(4)	0.02(2)	0.05(1)	0.26(2)	20.7(2)	0.29(3)	39.8(4)	0.43(4)	99.75	77.5	0.34	
				Opx (16)	0.209	55.0(4)	0.07(2)	0.8(2)	0.62(9)	13.8(5)	0.26(3)	27.0(3)	2.6(2)	100.15	77.5	0.33	
				Pig (6)	0.160	54.0(9)	0.14(5)	2.0(9)	0.78(7)	12(1)	0.29(3)	26(1)	4.9(4)	100.11	79.1	0.31	
				Metal	0.010	—	—	—	—	—	—	—	—				
ULM-12 *ULM + Fo75*	15	90	1200	Glass (7)	0.610	52(2)	0.65(5)	11.7(4)	0.25(8)	15.5(4)	0.28(6)	6.2(6)	12(2)	98.58	41.7		0.0782
				Pig (4)	0.074	53.7(6)	0.15(5)	1(1)	0.62(3)	15.7(2)	0.32(4)	24(1)	3.5(7)	98.99	73.5	0.26	
				Olivine (10)	0.235	38.2(6)	0.03(2)	0.06(1)	0.28(2)	20(2)	0.28(6)	41(1)	0.50(7)	100.35	78.8	0.19	
				Plag (2)	0.079	44(2)	—	29(7)	—	3(2)	—	3(3)	19.6(4)	98.60			
				Metal	0.010	—	—	—	—	—	—	—	—				
LMC-1 *ULM + Fo75 + CPX*	12	90	1230	Glass (66)	0.842	49.9(4)	0.8(1)	10.7(2)	0.46(7)	14.1(3)	0.25(4)	11.7(2)	11.9(2)	99.81	59.8		0.0125
				Pig (7)	0.055	54(1)	0.05(3)	0.6(3)	0.54(3)	11.3(5)	0.20(3)	30(1)	3.0(6)	99.69	82.4	0.32	
				Olivine (19)	0.087	39.0(5)	0.03(2)	0.04(1)	0.37(2)	17.0(3)	0.19(2)	42.8(6)	0.38(3)	99.81	81.7	0.33	
				Metal	0.017	—	—	—	—	—	—	—	—				
LMC-2 *ULM + Fo75 + CPX*	23	115	1230	Glass (26)	0.877	50.7(3)	0.8(1)	10.4(4)	0.38(7)	14.8(2)	0.22(5)	10.8(3)	11.7(2)	99.80	56.6		0.0263
				Pig (18)	−0.051	55.7(5)	0.08(4)	0.7(5)	0.61(6)	12.1(1)	0.18(2)	28.5(7)	2.8(4)	100.67	80.8	0.31	
				Olivine (6)	0.173	38.5(3)	—	0.04(1)	0.27(7)	18.7(2)	0.19(2)	41.4(3)	0.36(3)	99.46	79.8	0.33	
				Metal	t	—	—	—	—	—	—	—	—				
LMC-3 *ULM + Fo75 + CPX*	24	115	1200	Glass (16)	0.762	49.5(3)	0.8(1)	11.7(1)	0.38(8)	14.3(4)	0.18(4)	9.1(1)	12.8(2)	98.76	53.2		0.0151
				Pig (11)	0.081	54.4(5)	0.08(3)	0.9(1)	0.70(5)	13.3(2)	0.22(2)	26.0(6)	4.0(4)	99.60	77.8	0.32	
				Olivine (3)	0.154	38.5(9)	—	0.06(2)	0.35(2)	20.5(3)	0.27(2)	39.5(4)	0.42(2)	99.60	77.4	0.33	
				Metal	0.003	—	—	—	—	—	—	—	—				
LMC-4 *ULM + Fo75 + CPX*	23	90	1200	Glass (19)	0.762	49.7(3)	0.8(1)	11.7(2)	0.35(8)	13.8(3)	0.16(4)	9.5(1)	12.7(2)	98.71	54.9		0.0224
				Pig (11)	0.098	54.6(4)	0.09(3)	0.8(4)	0.6(1)	12.9(5)	0.22(2)	26.8(6)	3.7(4)	99.71	78.8	0.33	
				Olivine (3)	0.129	38.0(4)	—	0.03(2)	0.35(2)	20.0(3)	0.24(2)	40.9(4)	0.42(4)	99.94	78.5	0.33	
				Metal	0.011	—	—	—	—	—	—	—	—				
LMC-5 *ULM + Fo75 + CPX*	27	115	1185	Glass (24)	0.844	49.6(3)	0.9(1)	12.2(3)	0.31(5)	14.5(4)	0.21(4)	8.7(2)	12.6(2)	99.02	51.6		0.0496
				Olivine (8)	0.193	38.0(6)	—	0.10(2)	0.31(2)	21.7(2)	0.29(2)	39.0(5)	0.49(5)	99.89	76.2	0.33	
				Pig (14)	0.014	54.0(6)	0.11(3)	1.0(2)	0.65(7)	14.5(5)	0.25(3)	24.7(7)	4.6(8)	99.81	75.2	0.35	
				Metal	t	—	—	—	—	—	—	—	—				
				Plag (2)	q	45.4(5)	—	32.1(5)	—	1.8(6)	—	2.0(2)	17.3(5)	98.60			
LMC-6 *ULM + Fo75 + CPX*	24	55	1200	Glass (18)	0.782	50.5(4)	0.9(1)	11.6(3)	0.42(7)	15.0(4)	0.25(4)	8.8(5)	12.7(3)	99.87	51.0		0.0125
				Olivine (9)	0.184	38.0(6)	—	0.06(2)	0.38(2)	21.0(4)	0.21(4)	40.0(8)	0.42(4)	100.07	77.2	0.31	
				Pig (16)	0.383	54.8(6)	0.12(4)	1.0(3)	0.76(9)	12(1)	0.23(3)	27.7(8)	3.8(5)	100.41	81.0	0.24	
				Metal	t	—	—	—	—	—	—	—	—				
LMC-7 *ULM + Fo75 + CPX*	24	75	1200	Glass (78)	0.803	50.8(7)	0.8(1)	11.3(4)	0.34(7)	15.0(4)	0.17(4)	9.2(3)	12.6(2)	100.21	52.2		0.0308
				Olivine (10)	0.189	38.8(4)	—	—	0.37(3)	20(1)	0.22(3)	40.5(7)	0.42(6)	100.31	78.5	0.30	
				Pig (10)	0.083	55.2(3)	0.09(3)	0.6(2)	0.56(7)	13.5(6)	0.21(2)	26.9(5)	3.7(2)	100.76	78.0	0.31	
				Metal	t	—	—	—	—	—	—	—	—				

Table 2 (continued)

Exp # (bulk)	t (h)	P (bars)	T (°C)	Phase (#analysis)	% phase	SiO₂	TiO₂	Al₂O₃	Cr₂O₃	FeO	MnO	MgO	CaO	Total	mg#	$K_D^{phase/liq}$	SSR
LMC-8	26	115	1170	Glass (64)	0.707	49.2(3)	1.0(1)	12.8(2)	0.31(6)	14.8(3)	0.16(4)	8.2(2)	13.1(2)	99.57	49.5		0.0348
ULM + Fo₇₅ + CPX				Olivine (7)	0.156	38.3(5)	—	0.07(2)	0.30(1)	22.5(4)	0.23(3)	38.3(5)	0.51(5)	100.21	75.2	0.32	
				Pig (56)	0.137	54.0(6)	0.16(4)	1.2(4)	0.67(9)	14.0(7)	0.24(3)	24(1)	6(1)	100.27	75.5	0.32	
				Plag (12)	t	43.6(6)	—	34.5(9)	—	1.1(4)	—		0.6(5)	19.4(3)	99.20		
				Metal	t	—	—	—	—	—	—	—	—				
LMC-9	23	75	1170	Glass (33)	0.705	49.2(5)	0.9(2)	12.8(4)	0.33(6)	14.5(4)	0.22(4)	8.3(3)	13.1(2)	99.35	50.3		0.0739
ULM + Fo₇₅ + CPX				Oliv (22)	0.145	38.4(6)	—	0.05(2)	0.32(2)	21.6(5)	0.20(3)	38.8(7)	0.45(3)	99.82	76.2	0.32	
				Pig (15)	0.148	54.8(7)	0.16(4)	1.0(4)	0.68(8)	13.5(3)	0.18(4)	25.5(6)	4.7(5)	100.52	77.1	0.30	
				Metal	0.002	—	—	—	—	—	—	—	—				
LMC-10	22	115	1160	Glass (107)	0.798	49.1(4)	0.9(1)	12.4(5)	0.27(7)	15.3(3)	0.21(4)	8.1(8)	12.8(8)	99.08	48.4		0.0574
ULM + Fo₇₅ + CPX				Pig (19)	0.046	53.9(7)	0.16(9)	2(1)	0.72(9)	14.0(4)	0.23(3)	24(2)	5.4(9)	100.41	75.1	0.31	
				Oliv (12)	0.208	38.1(9)	—	—	0.26(2)	23.1(7)	0.20(2)	37(2)	—	98.66	73.9	0.33	
				Plag(5)	−0.031	45(1)	—	31(4)	—	2(1)	—	—	18(2)	96.00			
				Metal	−0.021	—	—	—	—	—	—	—	—				
LMC-11	14	75	1230	Glass (26)	0.823	51.9(4)	0.84	11.00	0.41	11.18	0.20	11.41	12.16	99.10	64.5		0.0240
ULM + Fo₇₅ + CPX				Pig (14)	0.015	56.7(5)	0.09(3)	0.5(1)	0.56(4)	8.8(8)	0.21(2)	30.7(8)	2.5(3)	100.06	86.1	0.29	
				Oliv(5)	0.115	40.1(2)	—	0.06(1)	0.33(8)	12.4(1)	0.17(2)	46.2(9)	0.37(5)	99.63	86.9	0.27	
				Metal	0.048	—	—	—	—	—	—	—	—				
LMC-12	18	90	1170	Glass (15)	0.754	49.8(2)	0.9(1)	12.2(4)	0.26(7)	15.2(6)	0.23(6)	8.4(9)	12.7(5)	99.69	49.6		0.1349
ULM + Fo₇₅ + CPX				Olivine (6)	0.165	36.9(3)	—	—	0.15(5)	22.0(3)	0.08(2)	39.8(2)	0.50(4)	99.43	76.3	0.31	
				Pig (2)	0.090	53.9(3)	.04(3)	0.14(6)	0.19(4)	15(1)	0.09(2)	25.8(5)	3.7(2)	98.86	75.1	0.33	
				Metal	0.009	—	—	—	—	—	—	—	—				
LMC-14	27	90	1185	Glass (7)	0.705	50(2)	0.6(1)	11(1)	0.07(4)	17(2)	0.11(4)	6(2)	12(1)		35.9		0.2369
ULM + Fo₇₅ + CPX				Olivine (4)	0.145	37.6(3)	0.05(1)	0.09(4)	0.13(2)	23(3)	0.13(2)	40(3)	0.59(8)		75.7	0.19	
				Pig (10)	0.148	53.6(5)	0.06(2)	0.6(1)	0.22(4)	16.0(9)	0.14(4)	26.1(6)	3.1(3)		74.4	0.20	
LMC-15	21	75	1185	Glass (8)	0.780	49.9(8)	0.82(9)	11.5(4)	0.4(1)	14.6(7)	0.18(6)	0.0(2)	12.6(2)		52.5		0.0195
ULM + Fo₇₅ + CPX				Olivine (5)	0.168	38.9(7)	—	0.06(1)	0.29(2)	19.5(2)	0.20(1)	40.4(7)	0.46(3)		78.7	0.30	
				Pig (8)	0.049	55.1(7)	0.11(3)	0.7(2)	0.56(8)	12.3(5)	0.22(2)	27.1(7)	4.1(4)		79.7	0.28	
				Metal	—	—	—	—	—	—	—	—	—				
LMC-16	19	110	1260	Glass (10)	0.869	50.1(3)	0.7(1)	10.5(1)	0.47(6)	14.0(3)	0.20(6)	11.4(2)	11.5(2)		59.3		0.0431
ULM + Fo₇₅ + CPX				Olivine (5)	0.128	39.5(5)	—	—	0.38(1)	17.3(4)	0.18(2)	42.7(7)	0.34(5)	100.40	81.4	0.33	
				Pig (7)	−0.009	56.2(4)	0.07(2)	0.4(1)	0.54(4)	10.0(4)	0.18(3)	30.2(4)	2.1(2)	99.69	84.3	0.27	
				Metal	0.012	—	—	—	—	—	—	—	—				
LMC-17	16	90	~1280[d]	Glass (14)	0.819	51.2(3)	0.8(1)	11.1(1)	0.45(9)	11.8(3)	0.19(3)	11.4(3)	12.1(1)	99.04	63.2		0.0380
ULM + Fo₇₅ + CPX				Pig (12)	0.048	56.4(7)	0.04(3)	0.2(1)	0.4(1)	9.5(4)	0.13(5)	31.6(6)	2.1(2)	100.37	85.6	0.29	
				Olivine (4)	0.091	38.2(6)	—	0.03(2)	0.20(3)	13.3(4)	0.09(2)	47.2(7)	0.29(4)	99.31	86.3	0.27	
				Metal	0.042	—	—	—	—	—	—	—	—				
LMC-18	9	75	~1280[d]	Glass (10)	0.826	52.8(4)	0.74(2)	10.9(1)	0.56(8)	9.1(2)	0.24(3)	12.8(2)	12.2(2)	99.34	71.4		0.0029
ULM + Fo₇₅ + CPX				Olivine (2)	0.076	40.6(6)	—	0.06(0)	0.41(0)	9.4(3)	0.16(1)	48.7(9)	0.37(1)	99.70	90.2	0.27	
				Pig (5)	0.027	56.4(5)	0.06(2)	0.3(2)	0.4(1)	7.5(2)	0.17(5)	32.7(8)	2.0(3)	99.53	88.7	0.32	
				Metal	0.071	—	—	—	—	—	—	—	—				
LMC-21	18	75	1185	Glass (12)	0.711	49.9(4)	0.9(1)	12.8(1)	0.40(6)	13.2(2)	0.19(6)	8.6(1)	13.1(2)	99.09	53.9		0.0861
ULM + Fo₇₅ + CPX				Olivine (5)	0.278	38.6(3)	—	—	0.36(6)	19.7(3)	0.21(2)	40.1(3)	0.6(2)	99.57	78.4	0.32	
				Pig (20)	0.146	54.9(7)	0.15(4)	1.1(3)	0.7(1)	12(1)	0.24(3)	25(1)	4.8(6)	98.89	78.6	0.32	
				Metal	0.021	—	—	—	—	—	—	—	—				

Run				Phase													
LMC-22 ULM + Fo₇₅ + CPX	21	75	1260	Glass (28)	0.772	49.1(4)	0.81(9)	12.1(1)	0.53(6)	12.5(3)	0.23(5)	11.6(3)	12.2(3)	99.07	62.1		0.2562
				Olivine (14)	0.027	39.1(4)	—	0.03(1)	0.36(3)	15.6(7)	0.15(3)	44.1(8)	0.34(5)	99.68	83.5	0.33	
				Pig (25)	0.172	56.0(4)	0.06(2)	0.5(1)	0.53(5)	10.5(5)	0.20(3)	30.0(8)	2.3(4)	100.09	83.6	0.32	
				Metal	0.037	—	—	—	—	—	—	—	—	—			
LMC-23 ULM + Fo₇₅ + CPX	12	90	1260	Glass (20)	0.888	52.0(3)	0.82(8)	10.3(2)	0.51(8)	13.0(3)	0.18(3)	12.3(2)	11.5(2)	100.61	62.8		0.0187
				Olivine (15)	0.128	39.0(5)	—	—	0.39(3)	15.8(5)	0.17(2)	44.4(8)	0.33(3)	100.09	83.3	0.34	
				Pig (9)	−0.047	56.0(6)	0.08(2)	0.5(2)	0.57(4)	11.5(4)	0.18(3)	29.2(4)	2.4(5)	100.43	81.9	0.37	
				Metal	0.026	—	—	—	—	—	—	—	—	—			
LMC-24 ULM + Fo₇₅ + CPX	15	115	1260	Glass (20)	0.923	50.4(2)	0.8(1)	9.8(1)	0.44(5)	14.7(4)	0.12(4)	11.5(2)	11.3(2)	99.06	41.9		0.0301
				Olivine (8)	0.168	39.1(3)	0.03(1)	0.03(1)	0.35(3)	18.2(2)	0.18(2)	42.2(7)	0.37(3)	100.46	80.4	0.34	
				Pig (12)	−0.084	55.6(5)	0.08(2)	0.5(1)	0.54(5)	12.2(4)	0.19(2)	28.8(6)	2.4(3)	100.31	80.9	0.33	
				Metal	t	—	—	—	—	—	—	—	—	—			
LMC-25 ULM + Fo₇₅ + CPX	23	90	1185	Glass (13)	0.710	49.8(2)	0.9(1)	12.6(1)	0.21(5)	14.9(4)	0.18(4)	8.3(2)	13.2(2)	100.09	49.8		0.0764
				Olivine (14)	0.149	37.8(4)	0.04(2)	0.07(3)	0.27(6)	22.7(3)	0.22(3)	39.1(3)	0.48(5)	100.68	75.4	0.32	
				Pig (19)	0.138	54.6(7)	0.15(7)	1.4(8)	0.72(7)	13.7(3)	0.23(2)	25(1)	4.8(8)	100.60	76.8	0.30	

a Number in parentheses indicates the number of analyses used for average.
b Number in parentheses is one sigma standard deviation in terms of least units cited. Therefore, 38.7(3) should be read as 38.7 ± 0.3 wt%.
c Element not analyzed of below detectability limit.
d Temperatures are estimated from power consumption levels during the experiment and verified using the Ol-Pig thermometer of Singletary and Grove (2003).
e Trace amounts present.

Microprobe analysis was performed using the MIT JEOL 733 Superprobes utilizing the appropriate glass and silicate standards. Crystal phases in the experiments were analyzed using a beam current of 10 nA, accelerating voltage of 15 kV, and a spot size of 2 μm. Glasses were analyzed under the same conditions but with a spot size of 10 μm to reduce the effects of small quench phases. The CITZAF correction package of Armstrong (1995) was used to reduce the data. The atomic number correction of Duncomb and Reed, the Heinrichs tabulation of absorption coefficients, and the fluorescence correction of Armstrong were used to obtain a quantitative analysis (Armstrong, 1995).

4. Experimental results

4.1. Approach to equilibrium

Experiments performed in this study are all synthesis experiments where crystals and melt have grown from an oxide mix. Phase appearance temperatures have not been reversed because past experience (Grove and Bence, 1977) indicates that direct synthesis is sufficient to recover equilibrium appearance temperature when significant (>40 wt%) melt is present. A materials-balance technique (Bryan et al., 1969) was used to estimate the phase proportions in the experimental products and to assess the gain or loss of material. The phase proportions and sum of squared residuals for each run are reported in Table 2. If no material was gained or lost during the experiment, the sum of squared residuals should be less than 1 (0 in the ideal case, Draper and Smith, 1966). A sum of squared residuals less than 1 is the first criterion for determination of a successful experiment.

A second criterion for equilibrium is the achievement of regular and consistent partitioning of major and minor elements between crystalline and melt phases. One measure of this criterion is the attainment of regular and consistent partitioning of Fe and Mg between olivine, pyroxene, and melt. The oliv–melt and pyroxene–melt Fe–Mg exchange distribution coefficients ($K_D^{Fe-Mg} = [X_{Fe}^{(Ol,Pyx)} X_{Mg}^{Liq}]/[X_{Mg}^{(Ol,Pyx)} X_{Fe}^{Liq}]$) are reported in Table 2. The reported Fe–Mg K_D values are well behaved and are similar to values reported for other systems (e.g., Singletary and Grove, 2003).

Consistent and regular behavior of the partitioning of minor elements between crystals and melt is also necessary for equilibrium. We calculated the partitioning of Ca, Al, Ti, and Cr between pyroxene and melt versus $1/T$ and compared it to the behavior found in the olivine–melt and pigeonite–melt models of Singletary and Grove (2003). This model used all published low-pressure experimental data on these partitioning reactions (see Singletary and Grove, 2003). We found that the behavior of the minor elements in our new experimental data matched that of the previous experimental data. Therefore, we proceed assuming the experiments are sufficiently close to equilibrium
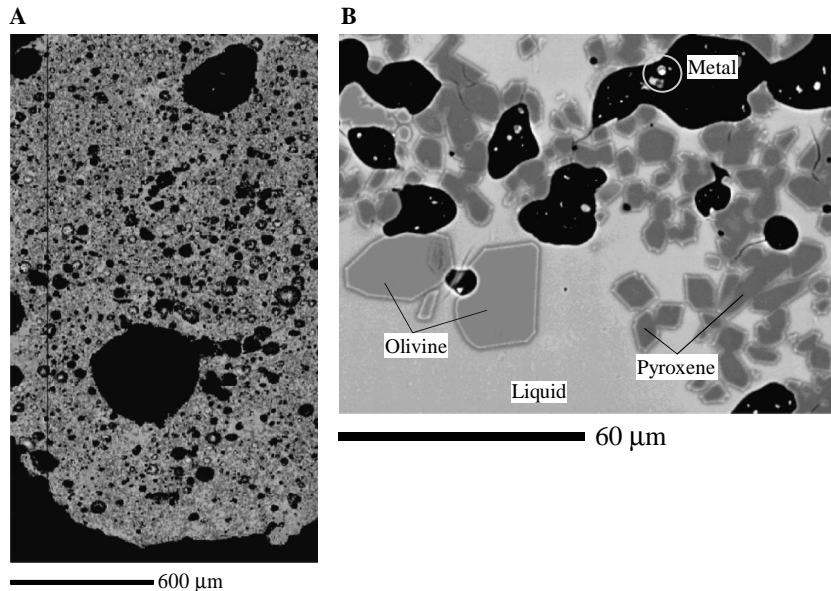
Fig. 2. Backscattered electron images of experimental run products. (A) BSE image of an entire experimental charge. Black areas within the charge are bubbles, presumably filled with CO gas during the experiment. (B) BSE image showing a close up of the crystalline run products and liquid. This experiment (LMC-3) is saturated with olivine, pigeonite, metal, and liquid.

based on the materials-balance calculations and systematic partitioning values.

To investigate smelting as it applies to ureilites, experiments were performed to obtain an assemblage of olivine, pigeonite, metal, and liquid with mg# of 75. Compositional, pressure, and temperature space were explored to obtain the correct assemblage and then to ascertain how the modal proportions of the phases may vary with mineral chemistry. The experimental results were then used to calibrate the coefficients of the smelting reaction for the ureilite appropriate bulk composition. The various bulk compositions used in this study are reported in Table 1.

4.2. Pu + Fo$_{83}$

The first bulk composition used in this study is a mix of a calculated liquid (Pu from Singletary and Grove (2003) see Table 1) and Fo$_{83}$ olivine in a ratio of 71:29. The amount of olivine was increased from that of the experiments reported in Singletary and Grove (2003) to obtain olivine saturation. The bulk composition plots to the left of the opx–cpx join in the Ol–Cpx–Qtz ternary diagram within the olivine primary phase volume.

Ten experiments were performed with this composition over a pressure range of 50–125 bars and temperatures of 1200–1280 °C. All runs at 125 bars are saturated with metal, olivine, pigeonite, and liquid. The mg#s for olivine and pigeonite decrease from 83 and 85 at 1280 °C to 78 and 79, respectively, at 1200 °C in a regular fashion. The Wo content ranges from 6.6 to 12.2. The pigeonites all plot along the opx–cpx join in the Ol–Cpx–Qtz ternary. The liquids plot along the olivine–pigeonite reaction boundary but below the 1-atm olivine–pigeonite–augite–liquid reaction point.

Two runs at 100 bars are also saturated with metal, olivine, pigeonite, and liquid. The mg#s of the olivine and pigeonite also decrease with decreasing temperature from 83 and 85 to 79 and 81, respectively. These are higher than those of the same phases at the same temperature at 125 bars. Olivine is absent from all experiments below 100 bars. Two experiments at 1230 °C; 80 bars and 1260 °C; 75 bars contain metal, pigeonite, and liquid as saturating phases. The mg#s of the pigeonite are higher than those at the same temperature but higher pressure and display the same decrease of mg# with decreasing temperature (87–85). Two experiments at 50 bars contain pigeonite, augite, metal, and liquid.

4.3. Pu + Fo$_{75}$

The second bulk composition is a mix of the calculated liquid in equilibrium with a Fo$_{83}$-bearing ureilite with 29% Fo$_{75}$ olivine added. Two experiments were performed with this composition at 1260 °C and pressures of 75 and 125 bars. The higher pressure run contains metal, olivine (Fo$_{78}$), pigeonite (mg#79), and liquid. The lower pressure experiment is saturated with augite, pigeonite, metal, and liquid. The pigeonite mg#s are slightly higher than those in the Pu + Fo$_{83}$ experimental set at the same temperature and pressure. All the pyroxenes plot along the opx–cpx join in the Ol–Cpx–Qtz ternary. The liquids plot near the calculated Pu composition.

4.4. ULM

A second equilibrium liquid (ULM) was calculated using the method of Singletary and Grove (2003). ULM is calculated to be in equilibrium with the silicate portion

of a ureilite with mg#s of 75–76 (Table 1). The bulk composition plots to the right of the opx–cpx join along the olivine–pigeonite reaction boundary.

Three experiments at 115 bars are saturated with pigeonite, metal and liquid. The mg# of the pigeonite decreases from 84.6 at 1260 °C to 72 at 1150 °C. The pigeonite plots along the opx–cpx join. The liquids plot along the olivine–pigeonite reaction boundary above the bulk composition but below that of the Pu liquid composition.

4.5. ULM + Fo₇₅

The fourth set of experiments uses a bulk composition of 71% ULM and 29% Fo$_{75}$. The addition of olivine pulls the bulk composition to the left of the opx–cpx join into the olivine primary phase volume. Six experiments span a temperature–pressure range of 1180–1300 °C and 75–125 bars. All of the runs are saturated with metal, olivine, orthopyroxene, and liquid. Mg#s of olivine and orthopyroxene range from 86 and 87, respectively, at 1230 °C; 75 bars down to 72 and 70 at 1180 °C; 110 bars. The pyroxene Wo contents vary from 2.2 to 9.6. As in the previous experiments, the mg#s decrease with decreasing temperature and increase with decreasing pressure.

The pyroxenes scatter along the opx–cpx join near the opx end. The liquids are more dispersed than in the previous experiments but scatter about the ULM bulk composition.

4.6. ULM + Fo₇₅ + CPX

The fifth bulk composition is a mixture of 76% ULM, 19% Fo$_{75}$ olivine, and 5% clinopyroxene with a mg# of 76. The bulk composition plots above the previous composition in the Ol–Cpx–Qtz ternary but still in the olivine primary phase volume (Fig. 3). Experiments were conducted from 50 to 115 bars and from 1160 to 1280 °C (Fig. 4). Twenty experiments with this bulk composition are saturated with metal, olivine, pigeonite, and liquid. Three experiments at 115 bars and below 1190 °C contain plagioclase as an additional saturating phase.

The olivine Fo content at 115 bars and 1280 °C is 81.4 and decreases to 73.9 at 1160 °C. At 90 bars, the high temperature experiment contains Fo$_{86.3}$ olivine. The Fo content decreases to 76.3 at 1175 °C. Olivine Fo contents at 75 bars decrease from 90.2 at 1280 °C to 76.2 at 1175 °C. One experiment at 55 bars, 1200 °C contains Fo$_{77.2}$ olivine.

Pigeonite mirrors the coexisting olivine with mg# decreasing with decreasing temperature and increasing with decreasing pressure. The experimental pyroxenes all plot along the opx–cpx join. The experimental liquids all cluster along the olivine–pigeonite reaction boundary, above the ULM liquid composition.

Several different bulk compositions were used in this study and there are similarities in all the experimental sets. Even though the experimental assemblages differ slightly,
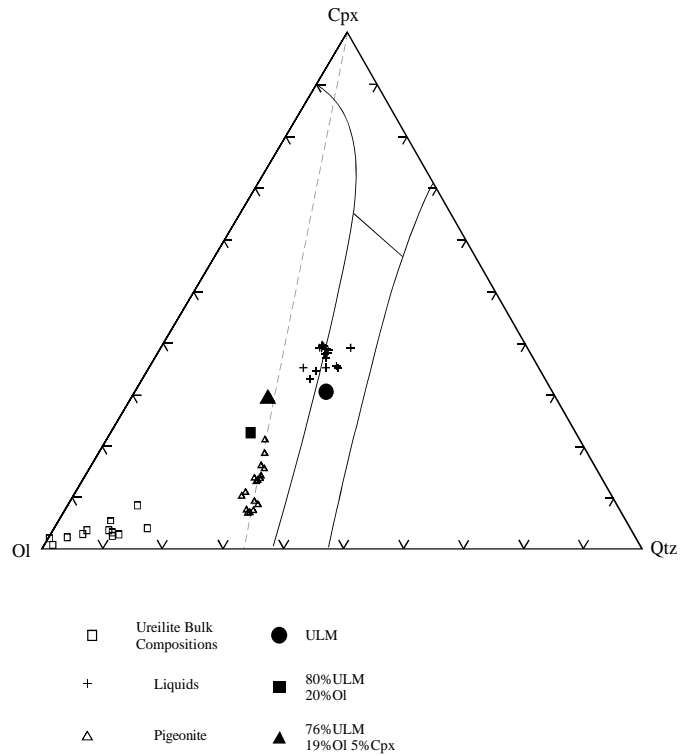

Fig. 3. Olivine–clinopyroxene–quartz ternary diagram. Phase boundaries are from Kushiro (1972) and are shown for reference. Run products for the ULM + Fo$_{75}$ + Cpx bulk composition are displayed, see text for discussion.
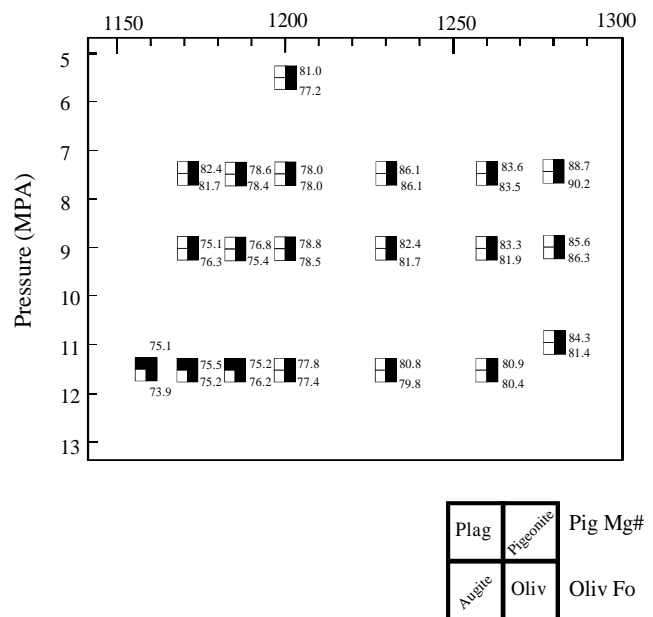

Fig. 4. Pressure–temperature grids for the ULM + Fo$_{75}$ + Cpx bulk composition. The bulk composition plotted is given in the upper right corner for each grid. Symbols for each experiments indicate saturating phases. Liquid is present in all experiments in addition to the crystalline phases. The phases present are represented by solid fill. Numbers by each symbol report the mg# of the phases.

they all display the same behavior in regards to the relationships between mg#, pressure, and temperature. As pressure decreases at constant temperature, the mg# of the silicate phases rises. Conversely, as temperature drops at constant pressure the mg# of the silicate phases drops.

4.7. Smelting reaction calibration

The experimental liquids were calculated to be in equilibrium with olivine and pigeonite on a reaction boundary, therefore they sample only a small interval of the smelting reaction. Since the bulk composition is dominated by the liquid, one of the phases will be exhausted after a small amount of crystallization. In the UPB, the bulk composition is dominated by olivine, which is consumed along with melt during the cooling and/or decompression that produced pigeonite and metal during smelting. In order to use the experimental data to model smelting in the UPB, it is necessary to calculate reaction coefficients from the experimental data, and to use these to model smelting. The coefficients are calculated in two ways—subtraction of modal proportions (SMP) and by mass balance (MB). The reaction is most sensitive to decreasing pressure, therefore, pairs of experiments at the same temperature and different pressures are used in the calculation. The SMP and MB methods give similar results, so we present only the MB method here.

The MB methods use pairs of experiments to calculate reaction coefficients. The analyses of all the experimental phases in the lower pressure experiment are mass balanced against the liquid of the higher pressure experiment to yield proportions of the phases that have been removed or added. The proportion of liquid after the mass balance is subtracted from 1 and the proportions of all the phases are then normalized to 1 liquid (Table 3). When the sums of both sides are within 10%, they are normalized to 1 for comparison (Table 4). The proportions of liquid, olivine, pyroxene, and metal are the only phases that are determined by the MB technique. The coefficients for C and CO in Eqs. (2)–(5) are determined by matching the estimated Fe with 1 mol of CO and C to balance the oxygen being released at the reaction boundary. The mole percents of each phase are then converted to weight percent.

Two calibration pairs at 1280 °C yield average smelting reaction coefficients of:

$$0.13\text{C} + 0.40\text{Ol} + 1\text{Liq} \Rightarrow 0.54\text{Pyx} + 0.63\text{Fe} + 0.32\text{CO} \quad (2)$$
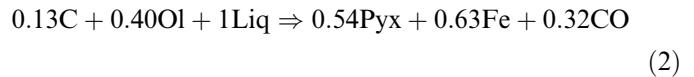
Three calibration pairs at 1260 °C give average coefficients of:

Table 3
Liquid normalized reaction coefficients (in wt%)

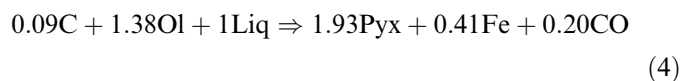| Temperature (°C)	ΔP	Bulk	C	+	Ol	+	Liq	$\Rightarrow$	Pyx	+	Fe	+	CO	10%
1280	40	LMC	0.18		0.56		1		0.35		0.88		0.44	Y
1280	25	LMC	0.08		0.24		1		0.72		0.37		0.19	Y
1260	15	LMC	0.02		0.93		1		1.92		0.09		0.04	Y
1260	40	LMC	0.04		0.86		1		1.62		0.17		0.07	Y
1260	25	Pu + Fo$_{83.8}$	0.05		0.52		1		1.32		0.23		0.12	Y
1260	25	LMC	0.11		0.68		1		0.62		0.53		0.27	N
1230	25	Pu + Fo$_{83.8}$	0.03		0.53		1		1.18		0.12		0.05	N
1230	50	ULM	0.07		1.11		1		1.79		0.33		0.16	Y
1230	40	LMC	0.13		0.65		1		0.98		0.61		0.30	Y
1230	25	LMC	0.07		2.37		1		3.03		0.30		0.15	Y
1230	15	LMC	0.24		2.00		1		2.14		1.11		0.56	N
1200	40	LMC	0.04		1.33		1		2.43		0.20		0.10	N
1200	15	LMC	0.08		1.71		1		2.66		0.35		0.18	N
1200	60	LMC	0.14		3.66		1		4.79		0.67		0.34	N
1200	35	LMC	0.20		3.88		1		4.47		0.92		0.46	N
1200	20	LMC	0.01		0.29		1		1.33		0.03		0.01	Y
1200	25	LMC	0.14		7.93		1		6.47		0.63		0.32	N

Table 4
Normalized smelting reaction coefficients

Temperature (°C)	ΔP	Bulk	C	+	Ol	+	Liq	$\Rightarrow$	Pyx	+	Fe	+	CO
1280	40	LMC	0.10		0.32		0.58		0.20		0.51		0.29
1280	25	LMC	0.06		0.18		0.76		0.55		0.28		0.17
1260	15	LMC	0.01		0.48		0.51		0.94		0.04		0.02
1260	40	LMC	0.02		0.45		0.53		0.85		0.09		0.06
1260	25	Pu + Fo$_{83.8}$	0.03		0.33		0.64		0.79		0.14		0.07
1230	50	ULM	0.03		0.51		0.46		0.79		0.14		0.07
1230	40	LMC	0.07		0.37		0.56		0.52		0.32		0.16
1230	25	LMC	0.02		0.69		0.29		0.87		0.09		0.04
1200	20	LMC	0.01		0.22		0.77		0.97		0.02		0.01

$$0.04C + 0.77Ol + 1Liq \Rightarrow 1.62Pyx + 0.16Fe + 0.08CO \tag{3}$$
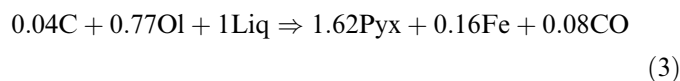
Three calibration pairs at 1230 °C yield:

$$0.09C + 1.38Ol + 1Liq \Rightarrow 1.93Pyx + 0.41Fe + 0.20CO \tag{4}$$

Even though seven experimental pairs are available at 1200 °C, only one has sums of both sides that are within 10%. The coefficients from that pair are:

$$0.01C + 0.29Ol + 1Liq \Rightarrow 1.33Pyx + 0.03Fe + 0.01CO. \tag{5}$$
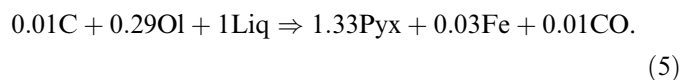
The normalized coefficients reported in Table 4 display a pattern of increasing metal production with increasing temperatures—dramatically so at 1280 °C.

5. Petrologic modeling

Petrologic modeling was performed to assess the behavior of a residue that is undergoing smelting. The smelting reaction is one that occurs only during cooling and/or decompression, and reactions are written with the smelted products (pigeonite and metal) on the right and the high temperature reactant assemblage (olivine + liquid) on the left. A bulk composition was depleted by subtracting olivine and liquid, and producing metal and pigeonite in proportions as determined by the smelting reaction coefficients calculated in the preceding section (Eqs. (2)–(5)). At each step, the compositions of the phases that are removed or added are calculated to be in equilibrium with the remaining liquid. Each model run was performed isothermally, and each step through the model corresponds to decompression and approximates fractional smelting. The compositions of the residue and liquid are recalculated after each step as phases are added and subtracted. It is possible that the smelting reaction will change as bulk compositions of the system change outside of the range of compositions that we were able to produce experimentally on the reaction boundary. As discussed below, we feel that these coefficients provide the best calibration currently available to model the dynamic process of decompression driven smelting.

The model inputs for each run include temperature, the proportions of olivine, metal, and pigeonite to add or subtract at the given temperature, a residue composition, and a liquid composition. Model runs were made using four temperatures for which the smelting reaction was calibrated and for which compositional data exist from the experimental data set—1280, 1260, 1230, and 1200 °C. An additional model run was made at 1300 °C using the compositions and coefficients from the 1280 °C experiments. Results for a typical model run are shown in Table 5. A bulk residue composition comprised of 91% Fo$_{75}$olivine, 7% liquid of the ULM composition, and 2% augite was deemed appropriate to the ureilites (see Section 6) and is

reported here. At each temperature, the composition of the highest pressure experimental liquid was used as the starting liquid composition. Olivine composition was determined by using a $K_D^{Fe–Mg}$ of 0.33 and assuming equilibrium with the liquid. The pigeonite composition is calculated using a temperature-dependent expression for Wo content determined from the experimental data (Fig. 5). The En and Fs components are calculated assuming equilibrium with the liquid. The Al, Cr, and Ti contents of the pyroxene are also predicted using temperature-dependent partition coefficients calculated from the experimental data (Singletary and Grove, 2003) (Fig. 6). The residues are plotted in Ol–Cpx–Qtz ternary space in Fig. 7 and olivine Fo contents are plotted against the number of model steps in Fig. 8.

Examination of the calculated residue compositions plotted in Ol–Cpx–Qtz ternary space shows that as smelting proceeds, the residue composition migrates toward the olivine–pigeonite reaction boundary at temperatures of 1260 °C and below. The 1200 and 1230 °C model residue trends pass above the ureilite bulk compositions. The 1260 °C model run passes directly through the ureilite model compositions and is the best fit to the bulk ureilite data using the 7% ULM:91% Fo$_{75}$:2% Cpx residue composition. At 1280 °C, the residue composition moves away from the reaction boundary and toward olivine (Fig. 7).

At temperatures above 1230 °C, the metal coefficients from the reaction calibration are such that the mg# of the silicate phases rises as the reaction proceeds. At 1200 °C, the amount of metal removed is small enough that the mg# of the silicate phases decreases as the reaction proceeds. The 1300 and 1280 °C model runs are the only ones that produce olivine Fo contents of 90 and above (Fig. 8).

5.1. Ca/Al ratios

Ureilite Ca/Al ratios are significantly above chondritic, previously reported as averaging $4.2 \times CI$ and as high as $14.5 \times CI$ (Goodrich, 1992). Using the modal proportions and mineral analysis reported in Singletary and Grove (2003) we recalculate the Ca/Al ratios and find an average bulk ratio of 7.1 with an upper value of 19.5. The bulk Ca/Al ratios are plotted versus the estimated temperature from Singletary and Grove (2003) in Fig. 9A. The data display two general, albeit scattered, trends—increasing Ca/Al ratio at temperatures below ∼1240 °C and decreasing Ca/Al ratios above 1240 °C.

The superchondritic Ca/Al values of the ureilites have always posed a problem for some models of ureilite petrogenesis. The cumulate model of ureilite petrogenesis requires the magma from which olivine and pigeonite precipitate have superchondritic Ca/Al ratios. Such a magma would indicate a plagioclase-depleted source material in the melting region and by inference some degree of igneous processing well before ureilite formation (Goodrich et al., 1987). The source material must also have superchondritic Ca/Al ratios in the residue model as well. Goodrich et al.

Table 5
Sample model output of isothermal decompression at 1260 °C

Step #	Phase		SiO₂	TiO₂	Al₂O₃	Cr₂O₃	FeO	MgO	CaO
Input	Residue		39.60	0.04	0.84	0.05	22.01	36.11	1.34
	Liquid		50.40	0.80	9.80	0.44	14.70	11.50	11.30
1	Olivine	Fo = 80.9	39.33	—	—	—	18.00	42.67	—
	Pigeonite		56.27	0.04	0.43	0.40	10.66	29.77	2.44
	Residue		38.83	0.04	0.81	0.06	21.40	34.65	1.35
	Liquid		50.80	0.83	10.11	0.44	14.68	11.56	11.59
2	Olivine	Fo = 81.0	39.34	—	—	—	17.91	42.75	—
	Pigeonite		56.28	0.04	0.43	0.40	10.60	29.82	2.44
	Residue		39.22	0.04	0.81	0.07	21.44	34.22	1.40
	Liquid		50.66	0.84	10.31	0.44	14.50	11.50	11.76
3	Olivine	Fo = 81.1	39.36	—	—	—	17.82	42.82	—
	Pigeonite		56.30	0.04	0.43	0.40	10.54	29.86	2.44
	Residue		39.57	0.04	0.81	0.08	21.47	33.82	1.45
	Liquid		50.51	0.86	10.52	0.43	14.32	11.43	11.93
4	Olivine	Fo = 81.2	39.38	—	—	—	17.73	42.90	—
	Pigeonite		56.31	0.04	0.43	0.40	10.49	28.90	2.44
	Residue		39.97	0.04	0.80	0.09	21.50	3.42	1.50
	Liquid		50.36	0.88	10.73	0.43	14.13	11.36	12.11
5	Olivine	Fo = 81.3	39.39	—	—	—	17.63	42.97	—
	Pigeonite		56.33	0.04	0.43	0.40	10.42	29.94	2.45
	Residue		40.33	0.04	0.80	0.10	21.53	33.03	1.54
	Liquid		50.20	0.89	10.95	0.43	13.94	11.30	12.30
6	Olivine	Fo = 81.4	39.41	—	—	—	17.53	43.05	—
	Pigeonite		56.34	0.04	0.43	0.40	10.36	29.99	2.45
	Residue		40.69	0.04	0.80	0.11	21.56	32.64	1.59
	Liquid		50.05	0.91	11.17	0.42	13.74	11.22	12.48
7	Olivine	Fo = 81.5	39.43	—	—	—	17.43	43.14	—
	Pigeonite		56.36	0.04	0.43	0.40	10.30	30.04	2.45
	Residue		41.04	0.04	0.79	0.13	21.59	32.27	1.63
	Liquid		49.88	0.93	11.40	0.42	13.55	11.15	12.67
8	Olivine	Fo = 81.6	39.45	—	—	—	17.33	43.22	—
	Pigeonite		56.38	0.04	0.43	0.40	10.23	30.08	2.45
	Residue		41.38	0.04	0.79	0.14	21.16	31.90	1.68
	Liquid		49.72	0.95	11.64	0.41	13.34	11.08	12.86
9	Olivine	Fo = 81.7	39.47	—	—	—	17.22	43.31	—
	Pigeonite		56.39	0.04	0.43	0.40	10.16	30.13	2.45
	Residue		41.71	0.04	0.79	0.14	21.64	31.54	1.72
	Liquid		49.55	0.97	11.87	0.41	13.14	11.00	13.06
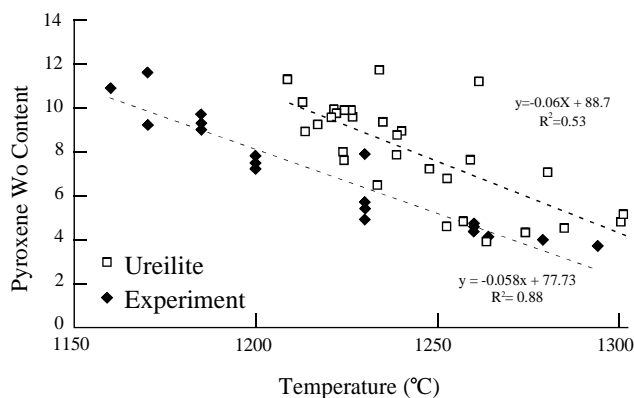
Fig. 5. Pyroxene Wo content versus temperature of experimental pyroxenes (see Table 2) and ureilite pyroxenes (data from Singletary and Grove (2003) and references therein).

(1999) demonstrated that in a single-stage melting model (<25–30% melting) to produce pigeonite-bearing residues, the source must have had Ca/Al ratios of 2.5 to 3 × CI.

The Ca/Al ratios for the model residue compositions are plotted in Fig. 10A versus the model step (or extent of smelting). Because all of the Ca and Al are carried in the pyroxene, the amount of pyroxene added to the residue dominates this value. The beginning value is slightly less than 1.5 and increases to over 2.5 at 1230 °C. The same behavior is observed in the temperature range of 1200–1260 °C. At 1280 °C, the Ca/Al ratios do not rise as rapidly and increase to just over 1.5. The same behavior is observed at 1300 °C with the rise in Ca/Al ratio increasing less than at 1280 °C. At high temperatures (>1280 °C) the values of the metal and pyroxene coefficients are such that less pyroxene is being added to the residue compared to
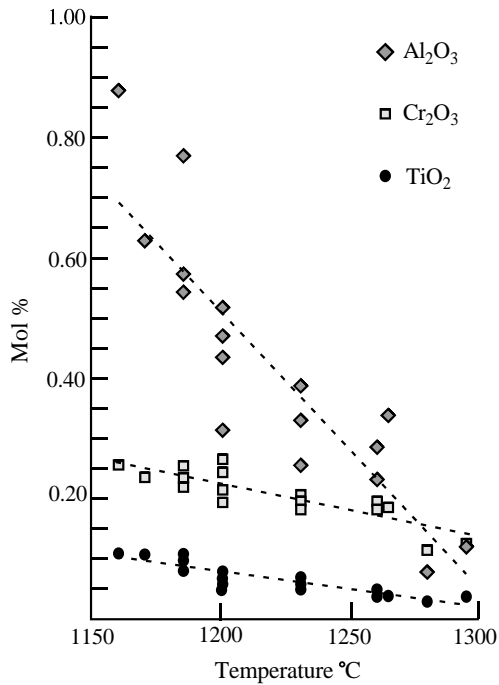
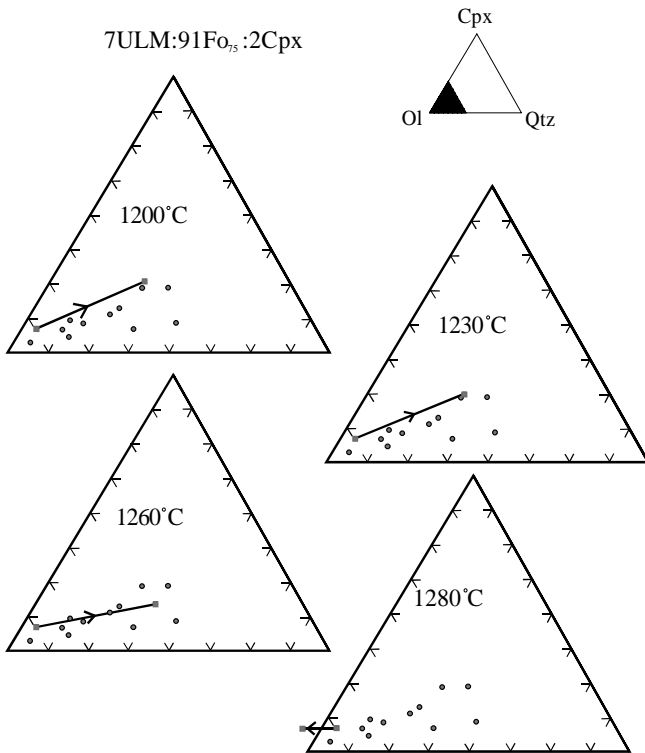Fig. 6. Experimental pyroxene compositions versus run temperature (see Table 2).

Fig. 7. Model residue compositions plotted in Olivine–clinopyroxene–quartz ternary space. Each diagram represents a portion of the Ol–Cpx–Qtz ternary as depicted in the inset. Filled circles are ureilite bulk compositions calculated from the modal proportions and phase analyses of Singletary and Grove (2003). Arrows display the predicted residue behavior during smelting at the indicated temperature. The starting composition is at the olivine-rich end and smelting drives the residue towards pyroxene-rich compositions. The exception is the 1280 °C trend which moves residue compositions away from the olivine–pyroxene reaction boundary.
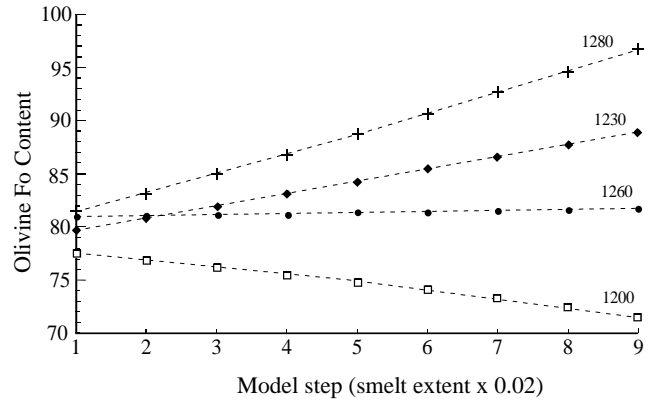
Fig. 8. Model olivine Fo content versus model step. Each step represents 2% fractional smelting as described in the text. Each trend represents isothermal decompression of the model residue composition.
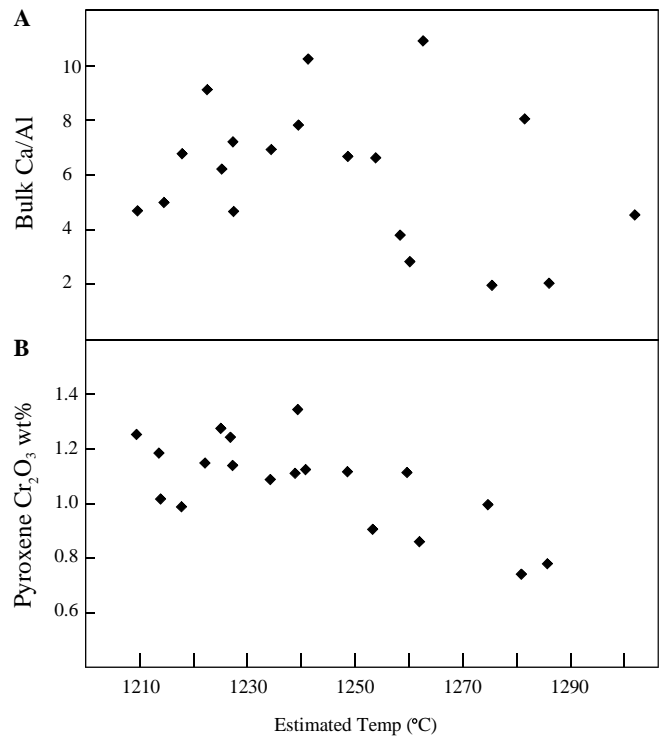
Fig. 9. (A) Ureilite bulk Ca/Al (molar) ratios versus estimated equilibrium temperatures. (B) Ureilite bulk Cr_2O_3 wt% values versus estimated equilibrium temperature (Singletary and Grove, 2003).

temperatures of 1260 °C and below. This indicates that pyroxene addition is the primary control on the model residue Ca/Al value.

5.2. Cr_2O_3

Ureilites are also characterized by high Cr contents (Mittlefehldt et al., 1998). The pyroxene Cr_2O_3 contents of ureilite olivine are plotted in Fig. 9B versus estimated temperature (Singletary and Grove, 2003). As seen in the Ca/Al data, there exist two trends. The pyroxene Cr_2O_3 wt% increases slightly at lower temperature and then trails off at high temperature (>1240 °C).
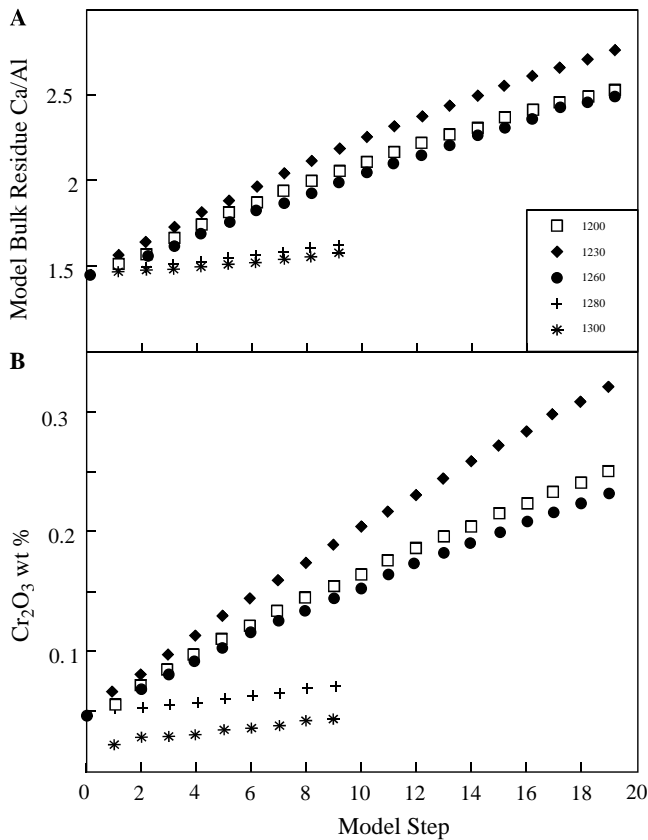
Fig. 10. (A) Model bulk residue Ca/Al (molar) values versus model step. (B) Model bulk residue Cr_2O_3 wt% values versus model step (see Fig. 8 for model).

The model residue Cr_2O_3 wt% is plotted in Fig. 10B versus the model step. As with the Ca/Al values, all Cr_2O_3 is hosted in the model pyroxene and therefore, pyroxene addition dominates the residue values. The initial Cr_2O_3 is ~0.05 and increases rapidly at 1230 °C to over 0.30 wt%. At 1280 °C, however, the increase in Cr_2O_3 increases minimally to just over 0.05 wt%. The Cr_2O_3 at 1300 °C drops initially and gradually rises, but the Cr contents never recover to the initial value.

6. Discussion

6.1. Experimental calibration of smelting

Reconnaissance experiments reported in Singletary and Grove (2003) were performed to explore the temperature–pressure relations of the smelting reaction using an approximation of a primary liquid composition reported by Goodrich et al. (2001). Experiments using that composition were not saturated with the correct phases and were too Mg rich to be generally relevant to the range of compositions spanned by ureilites. A second bulk composition was then calculated to explore more Fe-rich compositions using a liquid (Pu) calculated to be in equilibrium with an average ureilite containing Fo_{83} olivine. Experiments demonstrated that such a liquid with 20% Fo_{83} olivine add-

ed was saturated with pigeonite, augite, and metal (Singletary and Grove, 2003).

Experiments on the calculated liquid demonstrate saturation with olivine, pigeonite, metal, and liquid over the pressures and temperatures of interest when 29% Fo_{83} olivine is added. However, the lowest mg# of the experimental phases was 78. In order to produce olivine with lower Fo content, 29% Fo_{75} olivine was added to the mix in place of the Fo_{83} olivine. As before, the experiments are saturated with olivine, pigeonite, metal, and liquid. The lowest mg# again was 78.

A second equilibrium liquid (ULM) was then calculated using a subset of the ureilites with mg#s of 75–77. Experiments using the ULM liquid only are saturated with pigeonite, augite, metal, and liquid. Twenty-nine percent Fo_{75} olivine was then added to bring the bulk composition into the olivine primary phase volume. The bulk composition of 71% ULM and 29% Fo_{75} olivine is saturated with olivine, orthopyroxene, metal, and liquid with mg#s of the solid phases in the 75–76 range. The predominant pyroxene is orthopyroxene rather than pigeonite. In order to raise the Wo content of the experimental pyroxene, 5% Cpx with an mg# of 76 was added. The experimental pyroxenes produced by the Cpx added bulk composition (LMC) are pigeonite, with olivine, metal, and liquid as additional saturating phases.

The LMC bulk composition produces the correct assemblage with the appropriate mineral chemistry to explore smelting as it applies to the ureilites. Several other key data also support using this bulk composition. Fig. 5 displays the pigeonite Wo content of ureilites versus the estimated temperature as reported in Singletary and Grove (2003) and the experimental Wo content versus temperature from this study. The low temperature ureilites and experiments (~1150–1220 °C) contain Wo 8–12 pigeonite. The Wo content in both ureilites and experiments decreases at higher temperatures to ~4 at 1300 °C. The equations for the line of best fit through both sets of data are similar as well. Additionally, the pigeonite Wo content versus Olivine Fo content are similar between the LMC experiments and ureilites as shown in Fig. 11, with low olivine Fo contents
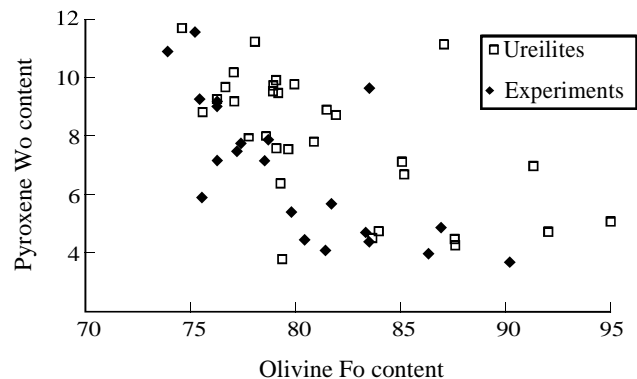

Fig. 11. Pyroxene Wo content versus olivine Fo content of experimentally produced pyroxene (see Table 2) and ureilite pyroxene, data from Singletary and Grove (2003).

correlating to high pigeonite Wo contents. Based on the similarity of the experimental data to the ureilite data, the correct phase assemblage, and mineral chemistry, we feel the LMC experiments represent a close approximation to the ureilite system. Consequently, these experiments are used to investigate the petrogenesis of the ureilites through smelting of a low Fo (75–77) residue.

6.2. Petrologic consequences of smelting

If smelting is occurring then several predictions can be made about mineral chemistry and the experiments should display systematic behavior consistent with the smelting reaction. If this is the case, then the experiments can be used to predict the consequences of smelting and then compared to the mineral chemistry variations in the ureilites. The smelting reaction occurs in association with the olivine–low Ca pyroxene reaction boundary (see Fig. 12). Therefore, the reaction can only proceed when there is: (1) isothermal decompression which leads to a rise in mg# of the silicate phases as smelting proceeds; or (2) isobaric cooling that leads to a decrease of mg#. The first process can lead to the observed compositional characteristics of ureilites, and the second process does not.

The 20 experiments shown in Fig. 4 exhibit this behavior. Along all isotherms, as pressure decreases, the olivine Fo content and pigeonite mg# rise (with the exception of two experiments at 1200 °C). Likewise, along each isobar, the mg# of both phases decreases. This set of smelted experiments can now be used to apply the smelting model to ureilites and investigate smelting as a viable model for ureilite petrogenesis.

The results of the smelting reaction coefficient calibration indicate that the smelting reaction is proceeding as hypothesized, with carbon, olivine, and liquid being consumed at the reaction boundary and carbon monoxide,
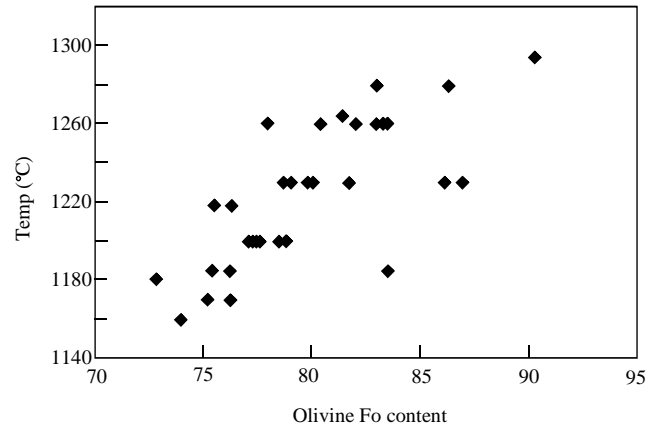

Fig. 13. Experiment temperature versus olivine Fo content. Data from this study (see Table 2.)

pigeonite, and metal being generated. There exists scatter in the data, but there is a general trend of increasing metal production with higher temperatures. This is reflected in Fig. 13 that plots Fo content of experimentally produced olivine against temperature.

The results of the model smelting runs indicate that if the ureilite source material contained Fo_{75} olivine, the ureilites are best modeled by progressive isothermal decompression of an olivine-rich residue, approximated in our model by a composition of 7% ULM:91% Fo_{75}:2% Cpx. The residue trend generated by fractional smelting indicates that the initial residue must be olivine rich to reproduce the bulk composition variations in ureilites. This is best illustrated in Fig. 7 in the Ol–Cpx–Qtz ternary diagram. The starting point for smelting is a source material that contains only olivine + carbon + melt. This source is produced once the temperature has risen to sufficiently high values (in excess of 1260 °C). At these temperatures the calibrated reaction coefficients become such that smelting can produce the high mg# (>90) ureilites and the smelted trend of ureilite residue compositions shown in Fig. 7 can also be produced.

6.3. Minor element consequences of smelting

The behavior of the Ca/Al ratios and Cr_2O_3 contents of the model residue are also indicative of progressive smelting of a partially melted source material. At low temperatures (<1260 °C) the model runs indicate that smelting can raise the Ca/Al ratio and Cr_2O_3 content of the residue. As temperature increases and the amount of pyroxene added to the residue is decreased and outpaced by metal, the change in Ca/Al ratio decreases and approaches a constant value. The same behavior is observed in the Cr_2O_3 data as well. The ureilite data reported in Fig. 9 are consistent with this idea. While the exact Ca/Al values do not match, we caution that the full extent of compositional space has yet to be explored (more Ca/Al-rich residues) nor have all phases that maybe participating in the smelting reaction been included and accounted for (i.e., spinel may play a sig-
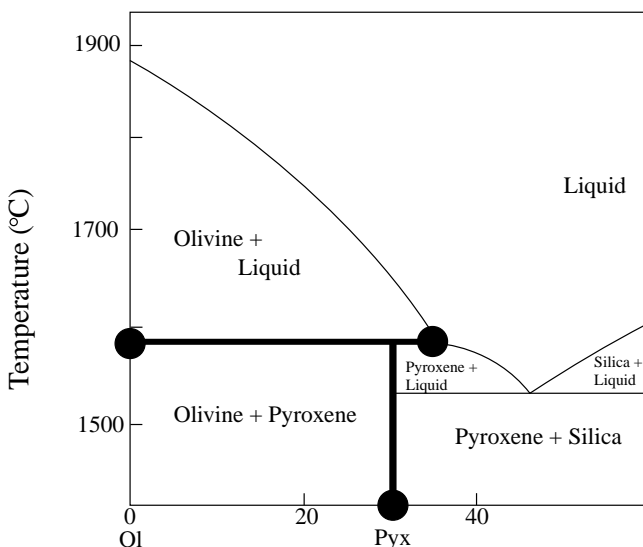

Fig. 12. Forsterite–silica binary phase diagram. The bold phase boundary indicates where the smelting reaction is occurring during cooling.

nificant role in controlling the Ca/Al ratio and Cr_2O_3 contents).

6.4. Smelting models: isothermal diapirism and degassing

The correlation of olivine Fo content with $\Delta^{17}O$ in ureilites (Fig. 14) has been interpreted to reflect a radial stratification in the ureilite parent body (Goodrich et al., 2003). Why such a gradient should exist is not clear. Based on the data presented here, we put forth an argument for a heterogeneous parent body that experiences diapirism as illustrated in Fig. 15.

Heterogeneous incorporation of heat producing elements, predominantly ^{26}Al in the form of calcium aluminum inclusions (CAIs), leads to differential heating of the ureilite parent body. As packages of material begin to heat temperatures rise and partial melting can begin. The heating process leads to the necessary starting point for ureilite smelting, which is the development of a source region of olivine + carbon + metal + melt. From this olivine-rich, melted body the smelting reaction can begin to operate and produce CO gas. Packages that are smelted become more buoyant as more gas is added and begin to rise. Note that this is a strongly exothermic crystallization reaction which releases latent heat of solidification of the olvine + melt to pigeonite crystallization reaction as well as the strongly exothermic reaction of C + O to CO (Richardson, 1974). The drop in pressure experienced by the ascending material drives the smelting reaction to produce ureilite residues with high mg# silicates. A process such as this would preserve the primitive isotopic signature of the ureilites and explain the correlation of high mg# to $\Delta^{17}O$ without the

need for a radial gradient in oxygen isotopes. This process would also retain metal and carbon that was present in the source, as they are carried along and retained in the source material. This model explains the inverse depth–temperature correlation reported by Singletary and Grove (2003). The smelting process also has the ability to enrich the Ca/Al ratios and Cr_2O_3 contents of the residue as displayed by the modeled residue compositions.

An alternative model that can lead to the same end result is crack-assisted decompression smelting. In this model there is no need to initiate diapiric ascent of a source region. Instead, the UPB develops pathways or "cracks" that allow the escape of CO gas. Once the gas begins to escape the smelting reaction (Eqs.(2)–(4)) proceed to the right, producing metal + pigeonite + CO gas and consuming C as olivine and liquid react at the peritectic. The result is a body containing heterogeneously distributed regions of variably smelted source material. The most smelted parts of the source in this body are regions from which gas could most efficiently escape.

It is possible that both of these processes operated on the UPB. An important characteristic of both models is that they occur after a melting episode that leads to the development of a parent body that contains olivine + liquid. The extent of melting is low (<10%; Singletary et al., 2005), so that primary nebular heterogeneities can be preserved in the variably melted parts of the parent body as they undergo smelting. The body is in an isothermal state; it has reached a maximum temperature which is recorded in the smelted ureilites of 1200–1300 °C and may be in the process of cooling in some regions. In fact, this stage of evolution of the body may be responsible for its ultimate disruption. Gas-bearing regions within the body that could not release their smelting generated CO pressure by diapirism or crack fed decompression may develop a high enough gas pressure to disrupt the body, thereby ending the smelting process and leading to the rapid cooling that is a characteristic feature of all ureilites.

7. Conclusions

Petrologic modeling, experimental results, and petrographic evidence support smelting as a viable process to invoke in ureilite petrogenesis. Smelting must begin with an olivine-rich source at low temperatures ($\sim$1200 °C) and occur over a restricted temperature range above 1200 °C and below 1300 °C. There is no requirement in this model that the source material be of uniform composition. If it is somewhat variable in terms of nebular major and trace element characteristics, a broad range of smelted residues can result, and models that invoke primary nebular processes (e.g., Takeda, 1987) can be reconciled with the overprinting petrologic process that we are proposing. The experimental assemblages indicate that ureilites with low mg#s (75–77) can be produced from a partially melted source that contained olivine + liquid + carbon + metal. The unmelted bulk material must have contained augite and possibly pla-
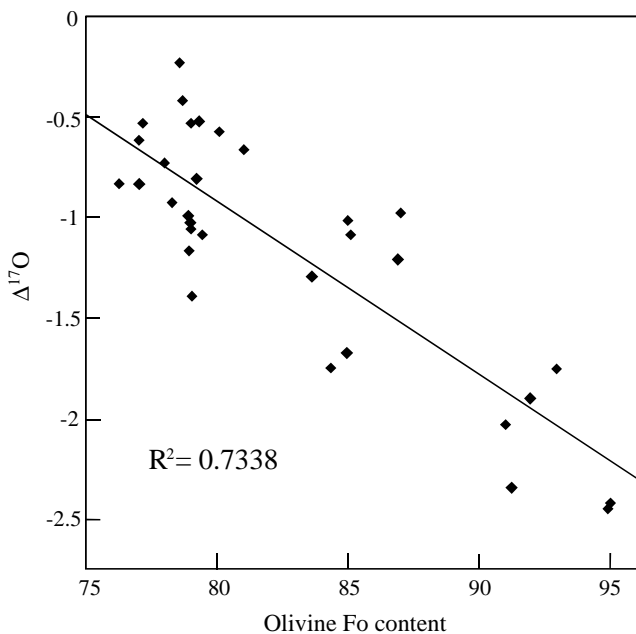

Fig. 14. Ureilite olivine Fo content versus $\Delta^{17}O$. Data from Singletary and Grove (2003) and Clayton and Mayeda (1988, 1996). Ureilites with lower $\Delta^{17}O$ values have higher olivine Fo contents, indicating an advanced degree of smelting.
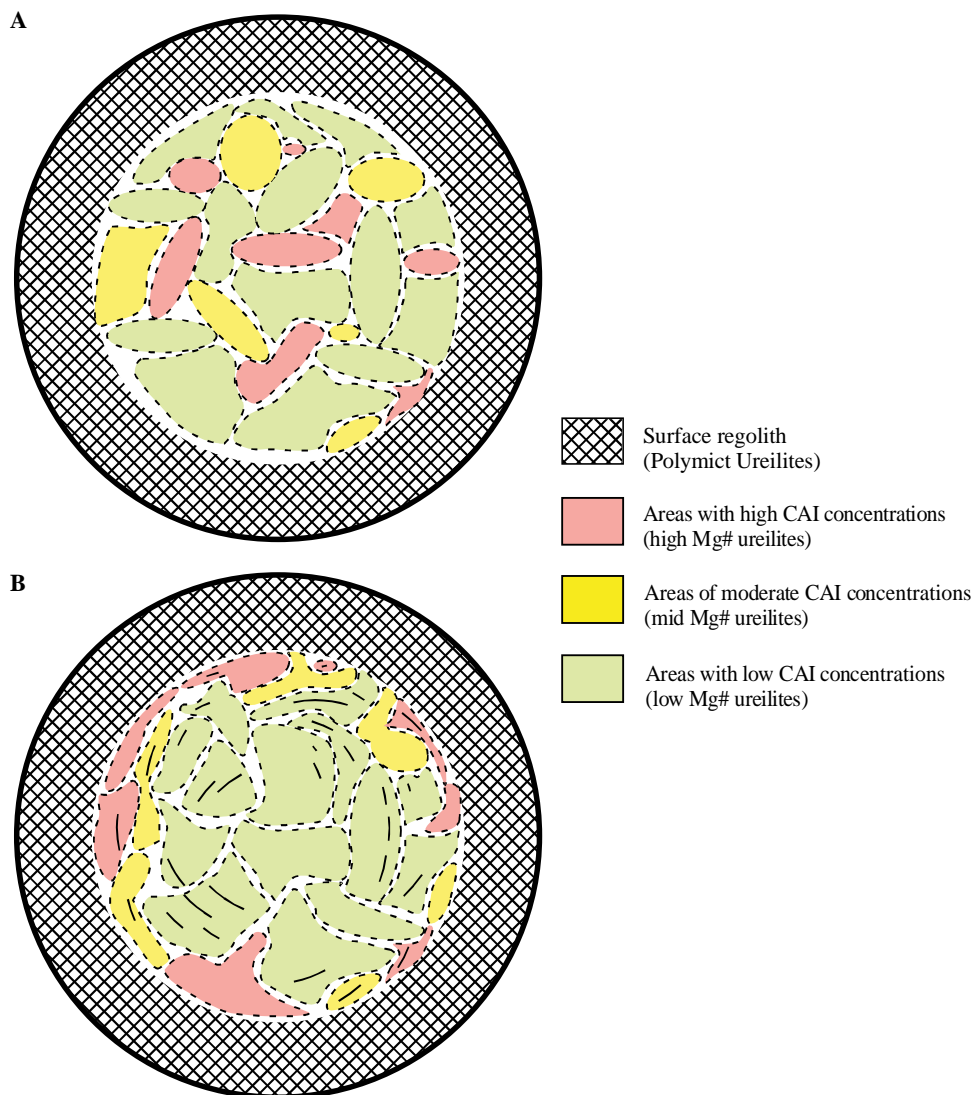
Fig. 15. Cartoon depicting the cross-section of a hypothetical ureilite parent body [UPB]. (A) Upper panel represents the UPB after the early stages of accretion before igneous processing begins. Heterogeneous accretion produces a parent body composed of randomly mixed packages of isotopically distinct material. Variable CAI contents lead to differential heat production due to the amounts of ^{26}Al present. (B) Lower panel shows the same UPB after igneous processing has begun and the early stages of differentiation of the UPB. Individual packages of material undergo differential heating that leads to variable degrees of smelting and ascent within the UPB. As packages of material reorganize within the UPB, mineral chemistries equilibrate and fabrics are produced.

gioclase. Fractional smelting took place under conditions of isothermal decompression where olivine, melt, and carbon are consumed by the smelting reaction and CO gas is produced along with pigeonite and metal. Gas production drives the smelting reaction either by diapirism or gas escape through fractures or open pathways in the parent body producing higher mg# residues that correlate to ureilites with mg#s greater than 90. The correlation of mg# to Δ^{17}O can also be explained by diapirism or variable smelting of regions open to gas escape. Thus, CAI-rich packages of material undergo increased amounts of smelting, negating the need for a UPB with a radial stratification of oxygen isotopes. The behavior of the model residue Ca/Al ratios and bulk Cr_2O_3 contents indicates that progressive heating of the ureilite source material may also explain the relations of Ca/Al ratio and Cr_2O_3 to temperature.

Acknowledgment

Associate editor: Alan D. Brandon

References

Armstrong, J.T., 1995. Citzaf—a package of correction programs for the quantitative electron microbeam x-ray-analysis of thick polished materials, thin-films, and particles. *Microbeam Anal.* **4**, 177–200.

Berkley, J.L., Gassaway-Brown, H., Keil, K., Carter, N.L., Mercier, J-C.C., Huss, G., 1976. The Kenna ureilite: an ultramafic rock with

evidence for igneous, metamorphic, and shock origin. *Geochim. Cosmochim. Acta* **40**, 1429–1437.

Berkely, J.L., Jones, J.H., 1982. Primary igneous carbon in ureilites: petrological implications. In: *Proceedings of the 13th Lunar and Planetary Science Conference. J. Geophy. Res.* **87**, A353–A364.

Berkley, J.L., Taylor, G.J., Keil, K., Harlow, G.E., Prinz, M., 1980. The nature and origin of ureilites. *Geochim. Cosmochim. Acta* **44**, 1579–1597.

Bryan, W.B., Finger, L.W., Chayes, F., 1969. Estimating proportions in petrographic mixing equations by least squares approximation. *Science* **163**, 926–927.

Boynton, W.V., Starzyk, P.M., Schmitt, R.A., 1976. Chemical evidence for genesis of ureilites, achondrite chassigny and nakhlites. *Geochim. Cosmochim. Acta* **40**, 1439–1447.

Clayton, R.N., Mayeda, T.K., 1988. Formation of ureilites by nebular processes. *Geochim. Cosmochim. Acta* **52**, 1313–1318.

Clayton, R.N., Mayeda, T.K., 1996. Oxygen isotope studies of achondrites. *Geochim. Cosmochim. Acta* **60**, 1999–2017.

Draper, N., Smith, H., 1966. *Applied Regression Analysis*. Wiley, New York, pp. 11–33.

Goodrich, C.A., 1992. Ureilites: a critical-review. *Meteoritics* **27**, 327–352.

Goodrich, C.A., Berkley, J.L., 1986. Primary magmatic carbon in ureilites: evidence from cohenite-bearing metallic spherules. *Geochim. Cosmochim. Acta* **50**, 681–691.

Goodrich, C.A., Fioretti, A.M., Molin, G., Tribaudino, M., 1999. Primary trapped melt inclusions in olivine in a ureilite—I. Description. *Lunar Planet. Sci.*, 30, abtr. 1026.

Goodrich, C.A., Fioretti, A.M., Tribaudino, M., Molin, G., 2001. Primary trapped melt inclusions in olivine in the olivine–augite–orthopyroxene ureilite Hughes 009. *Geochim. Cosmochim. Acta* **65**, 621–652.

Goodrich, C.A., Jones, J.H., Berkley, J.L., 1987. Origin and evolution of the ureilite parent magma: multi-stage igneous activity on a large parent body. *Geochim. Cosmochim. Acta* **51**, 2255–2273.

Goodrich, C.A., Krot, A.N., Scott, E.R.D., Taylor, G.J., Fioretti, A.M., Keil, K., 2003. Formation and evolution of the ureilite parent body and its offspring. In: *Lunar and Planetary Science XXXIII Abstract #1379*. Lunar and Planetary Institute, Houston (CD-ROM).

Grove, T.L., Bence, A.E., 1977. Experimental study of pyroxene–liquid interaction in quartz-normative basalt 15597. In: *Proceedings of the Lunar Science Conference*, vol. 8, pp. 1549–1579.

Mittlefehldt, D.W., McCoy, T.J., Goodrich, C.A., Kracher, A., 1998. Non-chondritic meteorites from asteroidal bodies. In: Papike, J. (Ed.), *Planetary Materials*, p. 36.

Kushiro, I., 1972. Determination of liquidus relations in synthetic silicate systems with electron probe analysis: the system forsterite–diopside–silica at 1 atmosphere. *Am. Mineral.* **57**, 1260–1271.

Richardson, F.D., 1974. *Physical Chemistry of Melts in Metallurgy*. Academic Press, London.

Rubin, A.E., 1988. Formation of ureilites by impact-melting of carbonaceous chondritic material. *Meteoritics* **23**, 333–337.

Scott, E.R.D., Taylor, G.J., Keil, K., 1993. Origin of ureilite meteorites and implications for planetary accretion. *Geophys. Res. Lett.* **20**, 415–418.

Sinha, S.K., Sack, R.O., Lipshutz, M.E., 1997. Ureilite meteorites: equilibration temperatures and smelting reactions. *Geochim. Cosmochim. Acta* **61**, 4235–4242.

Singletary, S.J., Grove, T.L., 2003. Early petrologic processes on the ureilite parent body. *Meteorit. Planet. Sci.* **38**, 95–108.

Singletary, S.J., Grove, T.L., Drake, M.J., 2005. Melting of Allende at pressures between 1 and 25 MPa. In: *68th Ann. Meeting Meteoritical Society Abstract # 5258*. Lunar and Planetary Institute, Houston (CD-ROM).

Takeda, H., 1987. Mineralogy of Antarctic ureilites and a working hypothesis for their origin and evolution. *Earth Planet. Sci. Lett.* **81**, 358–370.

Takeda, H., Mori, H., Ogata, H., 1989. Mineralogy of augite-bearing ureilites and the origin of their chemical trends. *Meteoritics* **24**, 73–81.

Treiman, A., Berkley, J.L., 1994. Igneous petrology of the new ureilites Nova 001 and Nullarbor 010. *Meteoritics* **29**, 843–848.

Vdovykin, G.P., 1970. Ureilites. *Space Sci. Rev.* **10**, 483–510.

Walker, D., Agee, C.B., 1988. Ureilite compaction. *Meteoritics* **23**, 81–91.

Walker, D., Grove, T., 1993. Ureilite smelting. *Meteoritics* **28**, 629–636.

Wasson, J.T., Chou, C.L., Bild, R.W., Baedecker, P.A., 1976. Classification of and elemental fractionation among Ureilites. *Geochim. Cosmochim. Acta* **40**, 1449–1458.

Weber, H.W., Begemann, F., Hintenberger, H., 1976. Primordial gases in graphite–diamond–kamacite inclusions from the Havero ureilite. *Earth Planet. Sci. Lett.* **29**, 81–90.